CrossMark

On the Diversity of Asymmetries in Gapped Protoplanetary Disks

Nienke van der Marel[1,8] , Til Birnstiel[2,3] , Antonio Garufi[4], Enrico Ragusa[5] , Valentin Christiaens[6] , Daniel J. Price[6] ,
Steph Sallum[7] , Dhruv Muley[1], Logan Francis[1] , and Ruobing Dong[1]

[1] Physics & Astronomy Department, University of Victoria, 3800 Finnerty Road, Victoria, BC, V8P 5C2, Canada; astro@nienkevandermarel.com
[2] University Observatory, Faculty of Physics, Ludwig-Maximilians-Universität München, Scheinerstr. 1, D-81679 Munich, Germany
[3] Exzellenzcluster ORIGINS, Boltzmannstr. 2, D-85748 Garching, Germany
[4] INAF, Osservatorio Astrofisico di Arcetri, Largo Enrico Fermi 5, I-50125, Firenze, Italy
[5] School of Physics and Astronomy, University of Leicester, Leicester, UK
[6] School of Physics and Astronomy, Monash University, VIC 3800, Australia
[7] Department of Physics and Astronomy, 4129 Frederick Reines Hall, University of California, Irvine, CA 92697-4575, USA
Received 2020 June 3; revised 2020 October 20; accepted 2020 October 20; published 2020 December 16

Abstract

Protoplanetary disks with large inner dust cavities are thought to host massive planetary or substellar companions. These disks show asymmetries and rings in the millimeter continuum caused by dust trapping in pressure bumps and potentially vortices or horseshoes. The origin of the asymmetries and their diversity remains unclear. We present a comprehensive study of 16 disks for which the gas surface density profile has been constrained by CO isotopologue data. First, we compare the azimuthal extents of the dust continuum profiles with the local gas surface density in each disk and find that the asymmetries correspond to higher Stokes numbers or low gas surface density. We discuss which asymmetric structures can be explained by a horseshoe, a vortex, or spiral density waves. Second, we reassess the gas gap radii from the ^{13}CO maps, which are about a factor of 2 smaller than the dust ring radii, suggesting that the companions in these disks are in the brown dwarf ($\sim$15–50 $M_{\rm Jup}$) or super-Jovian ($\sim$3–15 $M_{\rm Jup}$) mass regime on eccentric orbits. This is consistent with the estimates from contrast curves on companion mass limits. These curves rule out (sub)stellar companions ($q > 0.05$) for the majority of the sample at the gap location, but it remains possible at even smaller radii. Third, we find that spiral arms in scattered-light images are primarily detected around high-luminosity stars with disks with wide gaps, which can be understood by the dependence of the spiral arm pitch angle on disk temperature and companion mass.

1. Introduction

Protoplanetary disks around young stars are the birthplaces of planets, and their observed structures reveal the result of planet–disk interactions. Of particular interest are the so-called transition disks with large inner dust cavities ($>$20 au; e.g., Espaillat et al. 2014; van der Marel 2017). In this work, we use the term "transition disk" for any disk with a large cleared inner dust cavity ($>$20 au) as revealed by millimeter observations. The Atacama Large Millimeter/submillimeter Array (ALMA) has revealed a large diversity of structures in transition disks in both the dust (e.g., Pinilla et al. 2018b; van der Marel et al. 2019) and the gas (e.g., van der Marel et al. 2016b; Boehler et al. 2017; Dong et al. 2017), showing deep gas cavities well within the dust ring radii. The presence of these gas cavities is consistent with clearing by massive companions (either planetary or substellar) at wide orbits where the millimeter dust is trapped at the edge of the gap (e.g., Pinilla et al. 2012). Another proposed scenario for transition disk cavities is photoevaporation (Alexander et al. 2014), which is generally ruled out by the high accretion rates (Owen & Clarke 2012). Also, dead zones (low-viscosity regions due to poor ionization) have been proposed to generate transition disk cavities due to their sharp viscosity gradient (Regály et al. 2012), but the deep observed gas gaps cannot be reproduced by dead zones alone (Pinilla et al. 2016).

Some dust rings are highly asymmetric at millimeter wavelengths thought to be caused by azimuthal trapping (e.g., Birnstiel et al. 2013; van der Marel et al. 2013), but only a fraction of the transition disks are asymmetric. For a large sample of 38 transition disks, which are all known transition disks resolved at high spatial resolution with ALMA, the fraction of asymmetric disks is 24% (Francis & van der Marel 2020), but the completeness with respect to the total disk population cannot be determined. Regardless of the exact fraction, it remains unclear why azimuthal trapping only occurs in some of these disks.

The two main origins of azimuthal dust traps (azimuthal gas pressure maxima) are long-lived anticyclonic vortices caused by the Rossby wave instability (RWI) at the outer edge of the companion gap (e.g., Barge & Sommeria 1995; Zhu & Stone 2014) and gas horseshoes due to a pileup of material in eccentric cavities due to a binary companion (e.g., Ragusa et al. 2017) with a mass ratio requirement of $q > 0.05$. Whereas long-lived vortices require a low viscosity in the disk ($\alpha \lesssim 10^{-4}$) to survive (Godon & Livio 1999; Regály et al. 2012), horseshoes do not dissipate even at high viscosity (Miranda et al. 2017; Ragusa et al. 2020). Both scenarios produce an azimuthal gas overdensity of a factor of $\lesssim$2, which can trap millimeter-sized dust efficiently in the radial and azimuthal directions, resulting in a significant dust asymmetry (Birnstiel et al. 2013). Trapping efficiency increases with grain size up to a Stokes number of 1 (Birnstiel et al. 2013, 2016). The Stokes number St is defined (see Equation (1)) as the stopping time of a dust particle per orbital time and indicates

---

Table 1
Possible Scenarios for an Asymmetric Disk Caused by a Companion

Scenario	Required q Companion	Required α	Comoving/Trapping?	References
Vortex	>0.0002[a]	$\lesssim 10^{-4}$	Y	Zhu & Stone (2014); Dong et al. (2018a)
Horseshoe	>0.05	Any	Y	Ragusa et al. (2017)
Eccentric disk	0.003–0.05	Any	N	Ataiee et al. (2013)

Note.
[a] Based on a minimum of 68 $M_{\odot}$. The actual minimum mass estimate depends on the value of α; the listed value is derived for $\alpha \sim 10^{-4}$, as in Dong et al. (2018a).

how well dust grains are coupled to the gas. The gas overdensity itself comoves with the gas on a Keplerian orbit. A third possibility for a dust asymmetry is an eccentric disk. In contrast to a vortex or horseshoe, an eccentric disk caused by a massive companion (Kley & Dirksen 2006) does not comove with the gas (Ataiee et al. 2013) and thus does not trap millimeter dust; it acts as a "traffic jam" in their apocenter. The observed segregation between gas and dust consistent with trapping already rules out eccentricity as a major explanation for most observed asymmetric dust disks to date (Ataiee et al. 2013; van der Marel et al. 2016b). The differences between these three types of disks are summarized in Table 1.

Vortex dissipation due to dust feedback (e.g., Fu et al. 2014; Miranda et al. 2017) and slowly growing planets (Hammer et al. 2017) could potentially limit the vortex lifetime. Gas horseshoes are expected to survive for very long timescales (>7000 orbits), consistent with the disk lifetime (Miranda et al. 2017; Ragusa et al. 2020). A dissipation process would be a possible explanation for the low occurrence rate and diversity of asymmetries in transition disk rings, but this has not been quantified.

The main observable distinction between the vortex and gas horseshoe mechanisms is the companion mass and location; gas horseshoes require a mass ratio $q > 0.05$ (implying substellar rather than planetary mass), and the companion is closer to the star compared to the radial dust asymmetry location. It has been shown that HD 142527 hosts a (sub)stellar M dwarf companion with $M \sim 0.26\ M_{\odot}$ at an eccentric orbit between 18 and 57 au (Lacour et al. 2016; Claudi et al. 2019). Therefore, a horseshoe has been invoked to explain the asymmetry in the HD 142527 disk (Price et al. 2018). For most transition disks, it is unknown whether a companion, either planetary or (sub)stellar, is present inside the disk, particularly in the inner part.

The detection and quantification of companions in transition disks through direct imaging remains challenging due to the high contrast required to detect a companion in a dusty environment. Companion candidates have been debated in, e.g., HD 169142 (Biller et al. 2014; Ligi et al. 2018), LkCa15 (Sallum et al. 2015; Thalmann et al. 2016; Currie et al. 2019), HD 100546 (Quanz et al. 2013; Currie et al. 2015; Rameau et al. 2017), and MWC 758 (Reggiani et al. 2018; Wagner et al. 2019). The only robust detections of planetary companions in a transition disk to date are PDS 70 b and c (Keppler et al. 2018; Haffert et al. 2019). In most transition disks, no detections of companions have been found, and only upper limits have been derived. The low number of companion detections in transition disks has been suggested to be caused by uncertainties in expected planet brightness. If young planets are faint, they might only be detectable during the initial accretion phase while material is still flowing through the gap (Francis & van der Marel 2020) or during an episodic accretion outburst

(Brittain et al. 2020). Also, at distances close to the star (<0″.15), the achievable contrast remains limited.

Indirect evidence for companions is found in wide, deep gas gaps observed through CO isotopologue observations in transition disks (e.g., van der Marel et al. 2016b). The deep density drops and large separation between the gas cavity radius and dust ring radius already suggest that massive companions (>5 $M_{\rm Jup}$) must be responsible for the gaps (van der Marel et al. 2016b; Facchini et al. 2018b). Eccentric companions have been suggested to explain the wide separation between dust and gas cavity radius (Muley et al. 2019). The CO isotopologue images reveal a complete deficit of material close to the star in many transition disks (van der Marel et al. 2016b), which is generally modeled using a prescription of the surface density with a cavity depleted of gas all the way down to the center of the disk. This parameterization is inconsistent with the morphology of planet-induced gaps in planet–disk interaction models, which generally show a gap around the planet orbit but an undisturbed gas surface density profile inside the planet orbit (e.g., Fung & Chiang 2016; Facchini et al. 2018b). A fully cleared gas cavity would be more consistent with a more massive stellar companion, such as suggested for HD 142527 (Price et al. 2018), or perhaps multiple planets. However, for most CO observations of transition disks, the amount of gas inside the cavity (in particular close to the star) cannot be constrained due to the low spatial resolution, typically 0″.25 or ∼35 au, blending the contributions of the outer and inner gap edge, and a distinction between gas gap and cavity cannot be made (van der Marel et al. 2018a).

Other indirect evidence for companions is found through CO kinematics in disks of non-Keplerian motion: so-called "kinks" in the channel maps in between dust rings due to spiral density waves launched by the companion (e.g., Pinte et al. 2018, 2019), pressure perturbations (Teague et al. 2018), meridional flows (Teague et al. 2019), and warps in the inner cavity of the disk (e.g., Casassus et al. 2013; Boehler et al. 2017; Mayama et al. 2018). These warps can be explained by either misaligned inner disks or fast radial flows (Rosenfeld et al. 2014; Facchini et al. 2018a; Zhu 2019), although the reason could also be natal disk structure (Bate 2018). Also, spiral arms seen in scattered-light images have been linked to the presence of companions (Dong et al. 2015) and are often found in asymmetric disks (Garufi et al. 2018). Asymmetries have been proposed to trigger spiral arms (van der Marel et al. 2016a; Cazzoletti et al. 2018) or be part of them (Dong et al. 2018b; Rosotti et al. 2020), but there is no universal explanation for their coappearance.

With the large number of observed morphologies of asymmetries, rings, and spiral arms, it remains unclear how these different structures are connected to each other and whether the diversity is related to evolutionary, dynamical, or

stellar effects. In order to understand the diversity in disk structures, we present a sample study of 16 disks with and without asymmetries for a range of stellar, disk, and companion properties. We analyze the gas gap properties from spatially resolved CO observations and the Stokes numbers of dust grains throughout the disk and compare these with the dust properties. Furthermore, we compare the disk profiles with the limits of companion studies.

The paper is structured as follows. In Section 2, we present the sample selection based on a number of criteria and required data. We derive azimuthal profiles in the dust rings from ALMA archival continuum data in Section 3.1, gas gaps from ALMA CO observations in Section 3.2, and what is known about companions from direct imaging in Section 3.3. Using the combined information of gas and dust, we analyze in Section 4 the gas surface density profiles, the relevant Stokes numbers in asymmetries, and the properties of spiral arms. In Sections 5 and 6, we discuss the implications of our analysis and summarize our main conclusions.

2. Sample

We select a sample of disks with gaps, primarily transition disks, in order to constrain dust and gas properties across a range of azimuthal contrast and the presence of companions and spiral arms. In order to study the coupling of the dust to the gas, the measurement of the Stokes number is required, as larger Stokes numbers imply decoupling from the gas. The Stokes number is defined as the stopping time of a dust particle divided by the orbital time (Birnstiel et al. 2010). In the Epstein regime (where the ratio of the mean free path of the gas molecules λ_{mfp} to the grain size a_{grain} satisfies $\lambda_{mfp}/a_{grain} \geqslant 4/9$), the Stokes number is defined as

$$St = \frac{a_{grain} \rho_s \pi}{2 \Sigma_{gas}}, \qquad (1)$$

with ρ_s the intrinsic dust density (taken as $1 \, g \, cm^{-3}$) and Σ_{gas} the local gas surface density.

We thus require measurements of the gas surface density as a function of position in the disk. Gas surface density profiles can be derived from spatially resolved CO isotopologue data in combination with physical–chemical modeling in order to take into account freeze-out, (isotope-selective) photodissociation, and heating–cooling effects throughout the disk, e.g., DALI (Bruderer et al. 2012; Bruderer 2013). Parametric approaches of the abundance and temperature can be informative as well, in particular when multiple CO transitions are used, but larger uncertainties in the derived surface density profile remain.

We select transition disks for which the gas surface density has been derived using detailed CO modeling and resolved CO isotopologue observations, preferably a combination of ^{13}CO and optically thin $C^{18}O$. Furthermore, we require that the dust rings are at least marginally spatially resolved in the radial direction in order to make a proper assessment of the azimuthal structure in the dust.

The final sample thus consists of 14 transition disks (see Table 2), six of which show asymmetric features, and two ring disks without a large inner dust cavity. These two ring disks, TW Hya and HD 163296, were added to the sample for comparison, as dust rings in "full" protoplanetary disks are thought to behave in a similar way as transition disk rings with regard to dust trapping (van der Marel et al. 2019). Some known asymmetric transition disks had to be omitted due to a lack of high-resolution gas observations (e.g., V1247 Ori and HD 143006; Kraus et al. 2017; Andrews et al. 2018), whereas others did not have high-resolution dust continuum data (e.g., Sz 111, RY Lup, and LkHα 330; Isella et al. 2013; van der Marel et al. 2018a). The sample covers a range of stellar properties, with spectral types ranging from A0 to M2. Distances are taken from the Gaia DR2 (Gaia Collaboration et al. 2018). References for stellar properties are given in Francis & van der Marel (2020), where the stellar masses have been rederived using the updated Gaia DR2 distances.

For most of these disks, multiple ALMA programs are available in the ALMA archive. The programs with the best combination of spatial resolution and signal-to-noise ratio (S/N) are chosen for this study (see Table 2). The ALMA data reduction is described in Francis & van der Marel (2020) for the majority of the disks, and the table lists the reference where the data were first presented. For HD 163296, we use the fits file provided by the DSHARP team (Andrews et al. 2018), and for TW Hya, we use the fits file from Andrews et al. (2016). Table 2 also lists the derived radii of the dust inner disk from Francis & van der Marel (2020).

3. Data

3.1. Dust Structure

The ALMA continuum images of the samples are presented in Figure 1. All images have a high S/N; the median S/N of these images is 55, and the lowest S/N is 40. The azimuthal and radial profiles are extracted for each image using the position angle and inclination of the outer disk. As most asymmetric disks have a moderate to face-on inclination, optical depth effects are not considered to be affecting the results significantly. The only exception is IRS 48 with a 50° inclination, which implies that the continuum contrast might be overestimated by a factor of a few. The radial profiles are taken by averaging the ±30° on either side of the angle of the peak of the asymmetry, if present, or around the major axis position angle for axisymmetric disks. The radial profiles provide the radial locations of the dust rings, in combination with more detailed analysis from the literature (after correction for the new Gaia distances). These radii are also listed in Table 2 under the R_{dust} column. At each radial location, the azimuthal profile is extracted using a radial width of half the beam size. Figure 2 presents both the radial and azimuthal profiles after normalization, where the latter are split into asymmetric and nonasymmetric structures. In the asymmetric curves, the profiles are normalized to the flux at the opposite side of the asymmetric peak; in case of a nondetection on that side, a 3σ upper limit is assumed for the normalization. Note that disks with multiple rings appear multiple times, with one curve for each ring. In the radial plots, the deprojected beam profile is overplotted at the location of the dust ring to show how well the ring is resolved radially.

Contrasts in the asymmetric rings between the peak and the opposite side range from ~3 to 395. The disks of SR 21 and CQ Tau contain two asymmetric features along the same ring. The disk of SR 21 is not well resolved radially, and higher-resolution ALMA data show that these asymmetries are in fact more pronounced (Muro-Arena et al. 2020, T. Muto et al., in preparation). Also, for the CQ Tau disk, the asymmetries are moderate, and higher-resolution images (M. Benisty et al., in preparation) confirm that these asymmetric features are real.

Table 2
Sample Properties

Target	M (1)	λ_{obs} (mm) (2)	Program ID	R_{dust} (au) (3)	FWHM (deg) (4)	R_{ind} (au) (5)	PA (deg)	i (deg)	d (pc)	SpT	M_* ($M_\odot$) (6)	S (7)	C (8)	References (9)
IRS 48	A	0.9	2013.1.00100.S	70	58	⋯	100	50	134	A0	2.0	Y	⋯	1, 2, —
HD 142527	A	0.9	2012.1.00631.S	180	155	4.1	−20	27	157	F6	1.7	Y	Y	1, 3, 4
AB Aur	A	0.9	2012.1.00303.S	170	122	4.7	50	23	163	A0	2.6	Y	⋯	1, 5, —
MWC 758	A	0.9	2017.1.00492.S	50	49	3.0	62	21	160	A8	1.7	Y	C	6, 7, 8
				90	47									
HD 135344B	A	1.9	2016.1.00340.S	51	⋯	⋯	62	18	135	F4	1.4	Y	L	9, 10, 11
				79	96									
SR 21	A	0.9	2012.1.00158.S	36	⋯	⋯	24	15	138	G3	2.1	Y	L	12, 13, 13
				55	82									
				58	165									
CQ Tau	A	1.3	2017.1.01404.S	50	59	⋯	55	35	162	F2	1.7	Y	L	14, 15, 15
				50	59									
DoAr 44	S	0.9	2012.1.00158.S	47	⋯	⋯	60	20	146	K3	1.4	N	⋯	12, 16, —
J1604−2130	S	0.9	2015.1.00888.S	85	⋯	⋯	80	6	150	K2	1.0	N	L	17, 18, 19
LkCa 15	S	1.1	2015.1.00678.S	75	⋯	⋯	60	55	159	K2	1.3	N	C	20, 21, 22
PDS 70	S	0.9	2017.A.00006.S	74	⋯	10	−20	52	113	K7	0.9	N	Y	23, 24, 25
Sz 91	S	0.9	2012.1.00761.S	94	⋯	⋯	17	45	159	M1	0.6	N	L	26, 27, 27
HD 169142	S	1.3	2016.1.00344.S	25	⋯	2.2	5	13	114	F1	1.7	Y?	C	28, 29, 30
				60	⋯									
DM Tau	S	1.3	2017.1.01460.S	25	⋯	7.5	158	35	145	M2	0.5	⋯	⋯	31, —, —
HD 163296	S	1.3	2016.1.00484.L	14, 67, 100	⋯	⋯	132	42	102	A1	2.0	N	L	32, 33, 34
TW Hya	S	0.9	2015.1.00686.S	12, 29, 40	⋯	1.0	−25	6	60	M1	0.4	N	L	35, 36, 37

Note. Explanation of columns: (1) dust morphology (A = asymmetric, S = symmetric); (2) observing wavelength of the used dust continuum observations; (3) peak radius of the dust ring(s) in the disk; (4) azimuthal extent of the asymmetric feature along the dust ring from visibility analysis; (5) size of the inner dust disk, taken from Francis & van der Marel (2020); (6) stellar masses taken from Francis & van der Marel (2020), who derived them using Gaia DR2 distances and Baraffe et al. (2015) and Siess et al. (2000) evolutionary models; (7) detected spirals in scattered-light observations; (8) companions from direct imaging (Y = companion confirmed, C = companion candidate, L = no detection but limits available); (9) references for, respectively, ALMA data, spiral arms, and companions: (1) Francis & van der Marel (2020), (2) Follette et al. (2015), (3) Avenhaus et al. (2014), (4) Claudi et al. (2019), (5) Boccaletti et al. (2020), (6) Dong et al. (2018b), (7) Benisty et al. (2015), (8) Reggiani et al. (2018), (9) Cazzoletti et al. (2018), (10) Stolker et al. (2016), (11) Maire et al. (2017), (12) van der Marel et al. (2016b), (13) Muro-Arena et al. (2020), (14) Ubeira Gabellini et al. (2019), (15) Uyama et al. (2020), (16) Avenhaus et al. (2018), (17) Mayama et al. (2018), (18) Mayama et al. (2012), (19) Canovas et al. (2017), (20) Qi et al. (2019), (21) Thalmann et al. (2016), (22) Thalmann et al. (2010), (23) Keppler et al. (2019), (24) Müller et al. (2018), (25) Mesa et al. (2019a), (26) Tsukagoshi et al. (2019), (27) Maucó et al. (2020), (28) Pérez et al. (2020), (29) Gratton et al. (2019), (30) Reggiani et al. (2014), (31) Kudo et al. (2018), (32) Huang et al. (2018), (33) Muro-Arena et al. (2018), (34) Mesa et al. (2019b), (35) Andrews et al. (2016), (36) van Boekel et al. (2017), (37) Ruane et al. (2017).

Dust continuum asymmetries are marginally optically thick ($\tau \sim 0.5$, using the brightness temperature and the expected temperature at the dust ring location, which is computed using Equation (4) in Francis & van der Marel 2020), so the intensity contrasts do not directly correspond to the density contrasts. The symmetric rings show moderate azimuthal variations with values between 1 and 2 that may be optical depth effects in combination with the orientation of the disks or minor asymmetric dust traps.

Both MWC 758 and AB Aur show a clear indication of an eccentric dust cavity, as the inner dust disk detected in the ALMA continuum image is offset from the center of the disk.

The azimuthal contrast in the images cannot be compared reliably across the different images, as its value depends on the beam size and S/N along the ring. Instead, the asymmetries can be described reasonably well by 2D Gaussian profiles in the radial and azimuthal direction, where the FWHM is a measure of the asymmetric nature of the ring. Each asymmetric disk is fit in the visibility plane with a parameterized model $I(r, \phi)$, including such Gaussians. The visibility curves, parameterization, and best fits are given in Appendix A. For HD 135344B, a detailed visibility analysis was already performed by Cazzoletti et al. (2018). Using the σ_ϕ values, we compute the FWHM of

each asymmetric feature. For the axisymmetric disks, the FWHM is set to 360°. The FWHM is listed in Table 2.

3.2. Gas Structure

The CO isotopologue images of transition disks reveal that the gas cavity radii are well within the dust cavity radii. Gas surface density profiles have been derived from these CO images in order to quantify the depth and width of these gas gaps that can be used to derive information about possible embedded companions. Unlike the dust ring, which generally has a sharp inner edge due to the trapping (Pinilla et al. 2018b), the gas gap edge is not expected to be sharp, but it has been shown to have a gradual drop in density consistent with clearing by a companion, with the minimum at the location of the companion and the dust trapped at the outer edge. We have defined R_{dust} as a maximum in the intensity profile of dust emission (see previous section) and the location of the gas gap R_{gap} as the minimum in the gas surface density profile.

In model fitting of CO images, the gap in the surface density profile is usually parameterized (e.g., van der Marel et al. 2016b) in order to limit the number of free parameters. Unfortunately, the parameterization is not the same in different studies, and a comparison across the sample is challenging.
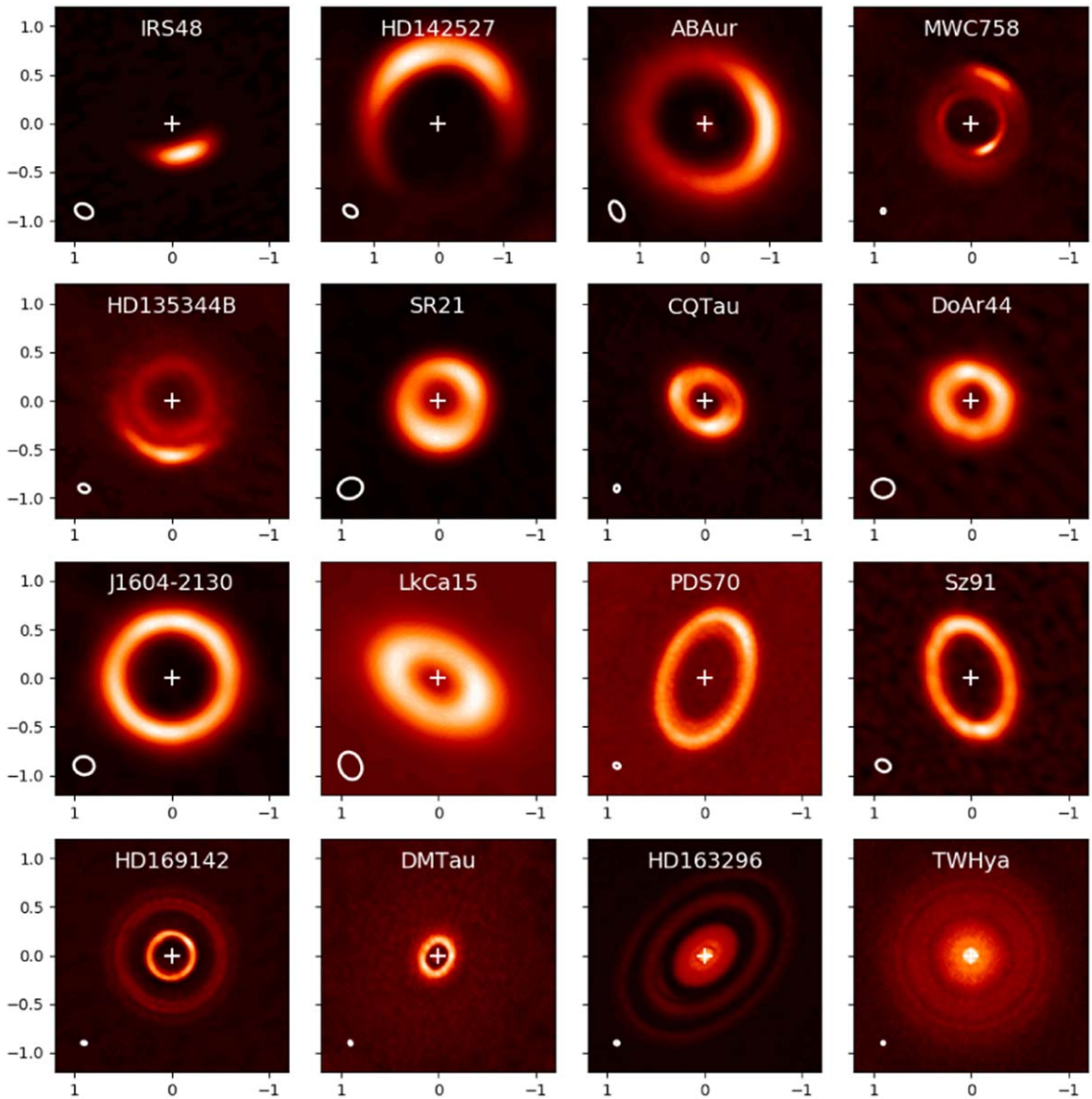
Figure 1. Gallery of ALMA continuum images at Band 6 or 7 of the disks in the sample of this study. The maps of HD 142527 and AB Aur are zoomed out compared to the others because of their size. Details of the observations can be found in Table 2.

Furthermore, the parameterization in early studies usually contained unphysical sharp edges at the gas cavity radii. Therefore, we reevaluate the gas surface density profiles and gap radii R_{gap} by analyzing the normalized azimuthal averaged intensity profiles of ^{13}CO for each target (Figure 3 and Appendix B). The properties and origin of each CO image are summarized in Table 3.

None of the ^{13}CO intensity profiles reveal a gap structure as expected from simple planet–disk interaction models; the minimum is located at the center of the disk. However, the spatial resolution of these images is limited (usually on the order of the size of the gap, $\sim 0\farcs2$–$0\farcs3$ or ~ 30–50 au), so the inner gas disk emission, if detected, is either unresolved (see also Figure 9 in van der Marel et al. 2018a) or lower than predicted by these models due to either a decrease in temperature, insufficient knowledge of processes inside the planet orbit leading to a further depletion of the gas, or both. Massive planets on eccentric orbits will significantly deplete the inner gas disk compared to regular planet–disk interaction

models, where planets are held fixed on circular orbits (Muley et al. 2019).

The deep, high-resolution ^{12}CO images of PDS 70 do reveal a clear gas gap (Keppler et al. 2019), and high-resolution dust continuum images reveal that inner dust disks are common in transition disks (Francis & van der Marel 2020), suggesting that in fact, many of these disks indeed harbor gaps rather than cavities. Also, the high accretion rates in transition disks (comparable to those of full disks) suggest a higher gas surface density close to the star (Manara et al. 2014; Francis & van der Marel 2020). Bosman et al. (2019) found evidence that the CO temperature in Herbig disks must be significantly lower than physical–chemical models predict to explain the ratios between different rovibrational lines. Such a decrease in temperature may also be a reason that ^{13}CO remains undetectable in the inner parts of the disk; thus, we assume in this study that all disks in fact harbor gas gaps.

In this work, we derive the gap location directly from the ^{13}CO profile across the sample. Since R_{gap} cannot be directly constrained
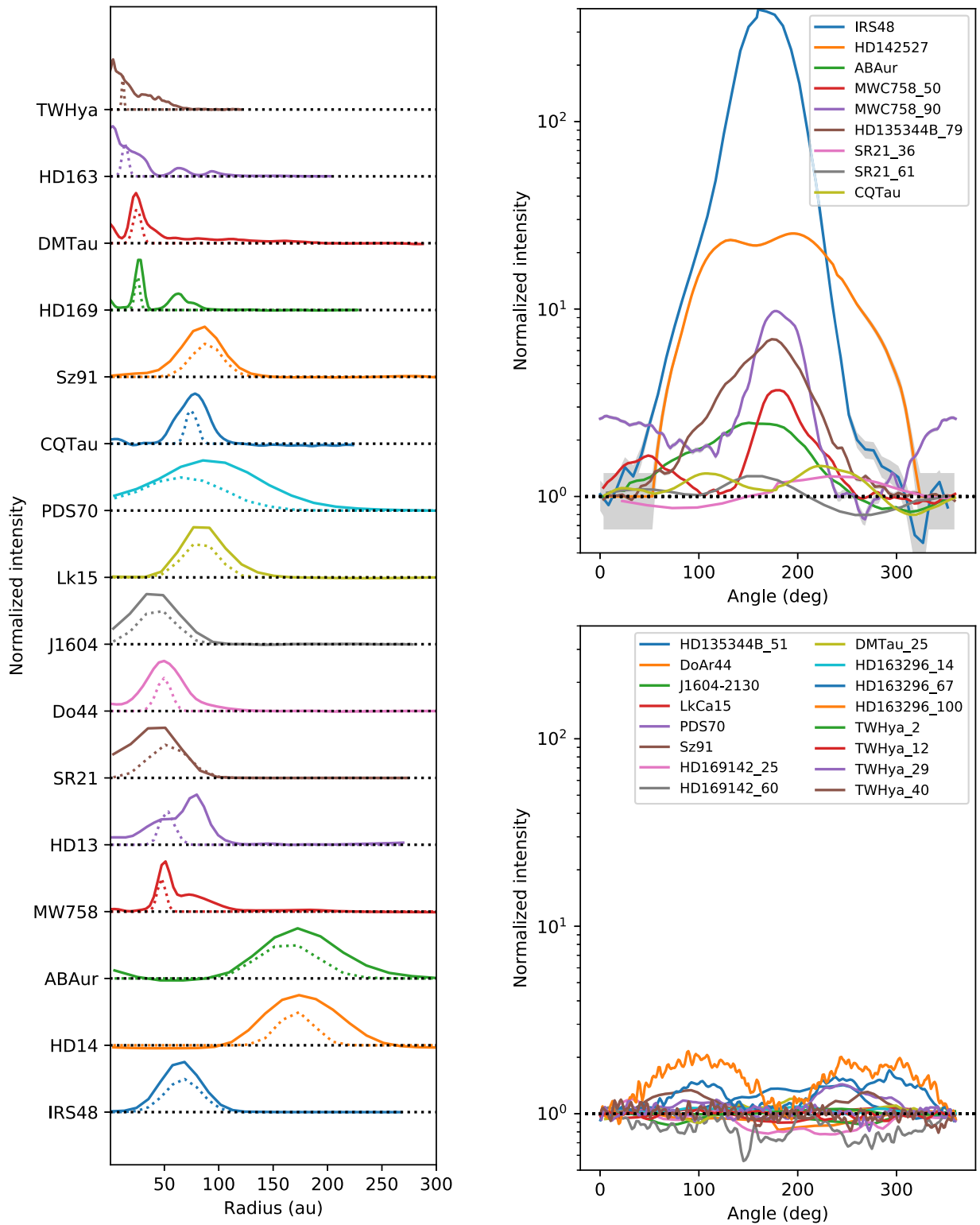
Figure 2. Intensity profiles along the radial (left) and azimuthal (right) directions at the location of the dust ring/asymmetry, normalized to the intensity at the opposite side of the asymmetry. The gray areas in the azimuthal plots indicate the noise level. In the left panel, the intensity profile is solid, while the average radial beam size is indicated with a dashed profile. The numbers in the azimuthal curves indicate the radius of the corresponding dust ring.

for all sources, we rely on two additional quantities, R_{CO} and R_{peak}, to infer it. In model simulations, the gap edge R_{CO} is defined (Rosotti et al. 2016; Facchini et al. 2018b) as the radius R where the normalized intensity $\bar{I}(R) < 1 - 0.66(1 - \bar{I}_{min})$. The low spatial resolution of our ^{13}CO observations does not allow us to measure this parameter directly, as the gap remains unresolved,

and it is unclear whether potential inner disk gas emission is confused or highly decreased. As an alternative, we measure the location of R_{peak}, the peak in the integrated ^{13}CO emission. Inspection of the results in Facchini et al. (2018b) shows that R_{peak} is approximately 1.4 times larger than R_{CO}. Figures 11 and 12 in Facchini et al. (2018b) provide the relations between R_{CO} and R_{gap}
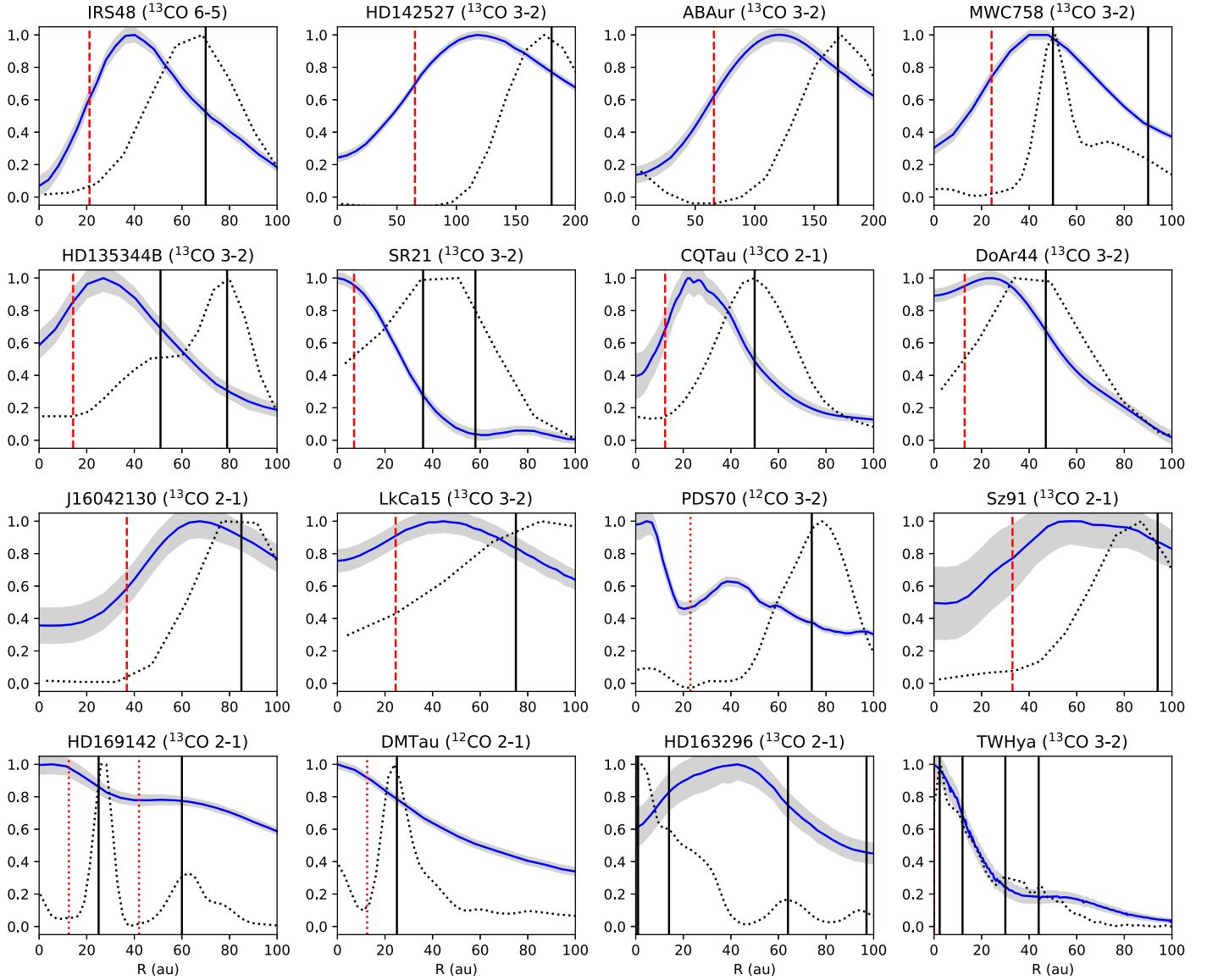
Figure 3. Normalized intensity profiles of ^{13}CO profiles of each target. The title indicates which line is used. Black dotted lines show the radial dust profiles, and black vertical lines indicate the locations of the dust ring(s). The gray area indicates the noise level. Red dashed lines indicate the derived gap radius R_{gap} (see text). Dotted red lines are used for targets where this analysis could not be done: for SR 21, the gap radius is taken from the analysis of the rovibrational CO line (Pontoppidan et al. 2008); for PDS 70, the gap radius is taken from the spatially resolved ^{12}CO profile (Muley et al. 2019); and for the last four targets, no information on the gap radius could be derived from the CO intensity profiles, and they are estimated to be located in between the dust rings.

and, for planet masses 5–15 M_{Jup}, the ratio $R_{CO}/R_{gap} = 1.3$. Using these relations, we derive the location of R_{peak}, R_{CO}, and R_{gap}, as listed in Table 3. The derived gap radii are well inside the dust cavity, typically at 10–20 au radius. If the relations between R_{peak} and R_{gap} are invalid because of eccentricity, R_{gap} is likely even further in. Unfortunately, no grid of models exists for planet–disk interaction models including eccentricity with predictions for the CO emission, so we have to make the assumption here that the radial gap shape remains similar. For SR 21, no gap was resolved in ^{13}CO, and the inner radius derived from the rovibrational emission (Pontoppidan et al. 2008) is assumed. For PDS 70, no ^{13}CO data are available, but the ^{12}CO profile directly reveals the gas gap in the image (Keppler et al. 2019). We notice that the ratios above still recover the gap radius at almost the exact same location for the R_{peak} of ^{12}CO in this case. For HD 169142, DM Tau, HD 163296, and TW Hya, no gas gaps were resolved, and the gap locations are estimated to be located in between the

dust ring radii. The drop in emission in the center of HD 163296 is caused by continuum oversubtraction (Isella et al. 2016).

Second, we present the first moment maps (velocity maps) of ^{12}CO data in Appendix C for each of our targets. A twist pattern (deviation from Keplerian rotation) in the inner part of the disk points toward a misalignment between the inner and outer disk, or a warp. Such a misalignment can be explained by the presence of a massive companion ($>1~M_{Jup}$) that breaks the disk, leading to a different precession of the inner and outer disk (e.g., Facchini et al. 2018a; Zhu 2019). An even stronger misalignment can be induced as a result of a secular resonance between the companion and the disk (Owen & Lai 2017). Also, radial flows of gaseous material from the outer to the inner disk have been proposed to explain the twist pattern (e.g., Price et al. 2018), but it is almost impossible to distinguish observationally from a misalignment (Rosenfeld et al. 2014) and not unique for substellar companions such as found in

Table 3
Gas Gap Properties

Target	ALMA Program	Line	Beam Size (arcsec)	R_{peak} (au) (1)	R_{CO} (au) (2)	R_{gap} (au) (3)	R_{gascav} (au) (4)	Σ_{acc} (1 au) ($\times 10^3$ g cm^{-2}) (5)	Ref. CO Analysis (6)
IRS 48	2013.1.00100.S	^{13}CO 6-5	0.19×0.15	40	29	22	31	0.80	1
HD 142527	2011.0.00318.S	^{13}CO 3-2	0.61×0.48	118	84	65	50[a]	7.70	2
AB Aur	2012.1.00303.S	^{13}CO 3-2	0.37×0.23	117	84	64	98	26.00	3
MWC 758	2012.1.00725.S	^{13}CO 3-2	0.22×0.19	40	29	22	20[a]	9.10	4
HD 135344B	2012.1.00158.S	^{13}CO 3-2	0.26×0.21	27	19	15	28	9.50	1
SR 21	2012.1.00158.S	^{13}CO 3-2	0.23×0.19	...	...	7[b]	7	2.90	1
CQ Tau	2017.1.01404.S	^{13}CO 2-1	0.15×0.15	23	16	13	20	1.00	5
DoAr 44	2012.1.00158.S	^{13}CO 3-2	0.31×0.29	26	19	14	24	1.90	1
J1604–2130	2013.1.01020.S	^{13}CO 2-1	0.28×0.24	68	49	37	35[a]	0.10	6
LkCa 15	2012.1.00870.S	^{13}CO 3-2	0.28×0.21	45	32	25	35	1.20	7
PDS 70	2017.A.00006.S	^{12}CO 3-2	0.08×0.06	41	29	23	22[c]	0.04	8
Sz 91	2013.1.01020.S	^{13}CO 2-1	0.25×0.22	52	37	29	32	0.58	9
HD 169142	2013.1.00592.S	^{13}CO 2-1	0.37×0.22	...	...	12, 42[d]	60	2.90	10
DM Tau	2017.1.01460.S	^{12}CO 2-1	0.10×0.10	...	...	12[d]	...	1.40	11
HD 163296	2013.1.00601.S	^{13}CO 2-1	0.27×0.19	...	...	...	...	7.60	12
TW Hya	2012.1.00422.S	^{13}CO 3-2	0.54×0.35	...	...	...	...	0.32	13

Notes. Explanation of columns: (1) radial peak of ^{13}CO emission (or ^{12}CO when ^{13}CO is not available) at the outer edge of the gas gap; (2) gas gap edge, as derived from R_{peak} and the relations in Facchini et al. (2018b); (3) gas gap minimum, as derived from R_{peak} and the relations in Facchini et al. (2018b); (4) gas cavity edge from the parameterized gas surface density model from the literature, corrected for the Gaia DR2 distance; (5) gas surface density at 1 au, using the accretion rate and Equation (2); (6) reference of the analysis of the CO isotopologues from the literature: (1) van der Marel et al. (2016b), (2) Boehler et al. (2017), (3) Piétu et al. (2005), (4) Boehler et al. (2018), (5) Ubeira Gabellini et al. (2019), (6) Dong et al. (2017), (7) N. van der Marel et al. in preparation, (8) Muley et al. (2019), (9) van der Marel et al. (2018a), (10) Fedele et al. (2017), (11) L. Francis et al. in preparation, (12) van der Marel et al. (2018b), (13) Kama et al. (2016a).
[a] Derived from threshold detectability of ^{12}CO at 10^{-2} g cm^{-2}.
[b] Derived from rovibrational CO line (Pontoppidan et al. 2008).
[c] Derived from resolved ^{12}CO profile (Keppler et al. 2019).
[d] Estimated from dust ring locations.

HD 142527, as lower-mass companions can result in radial flows as well (Calcino et al. 2020). Misalignment has been discovered independently in several targets through shadows (e.g., Marino et al. 2015), dippers (e.g., Ansdell et al. 2016), and direct measurements of the inner dust disk orientation (e.g., Francis & van der Marel 2020).

For the targets in this study, a warp was confirmed for four targets that were previously found in the literature: IRS 48, HD 142527, MWC 758, and J1604–2130. Also, AB Aur appears to show non-Keplerian motion on larger scales, but this is most likely due to the strong contributions from the spiral arms detected in ^{12}CO (Tang et al. 2017). For the other disks, no warp was detected, but we present a comprehensive overview of the properties of the observations suggesting that warps are impossible to detect with the available spatial/spectral resolution (Table 6). The table also provides references for other studies suggesting misalignment based on other data. Overall, all targets possibly have a misalignment between the inner and outer disk, pointing toward the presence of a massive companion. Derivation of the mass of the companion requires detailed knowledge of the viscosity, scale height, and precession time (Figure 12 in Zhu 2019), so no quantitative information can be derived from these maps.
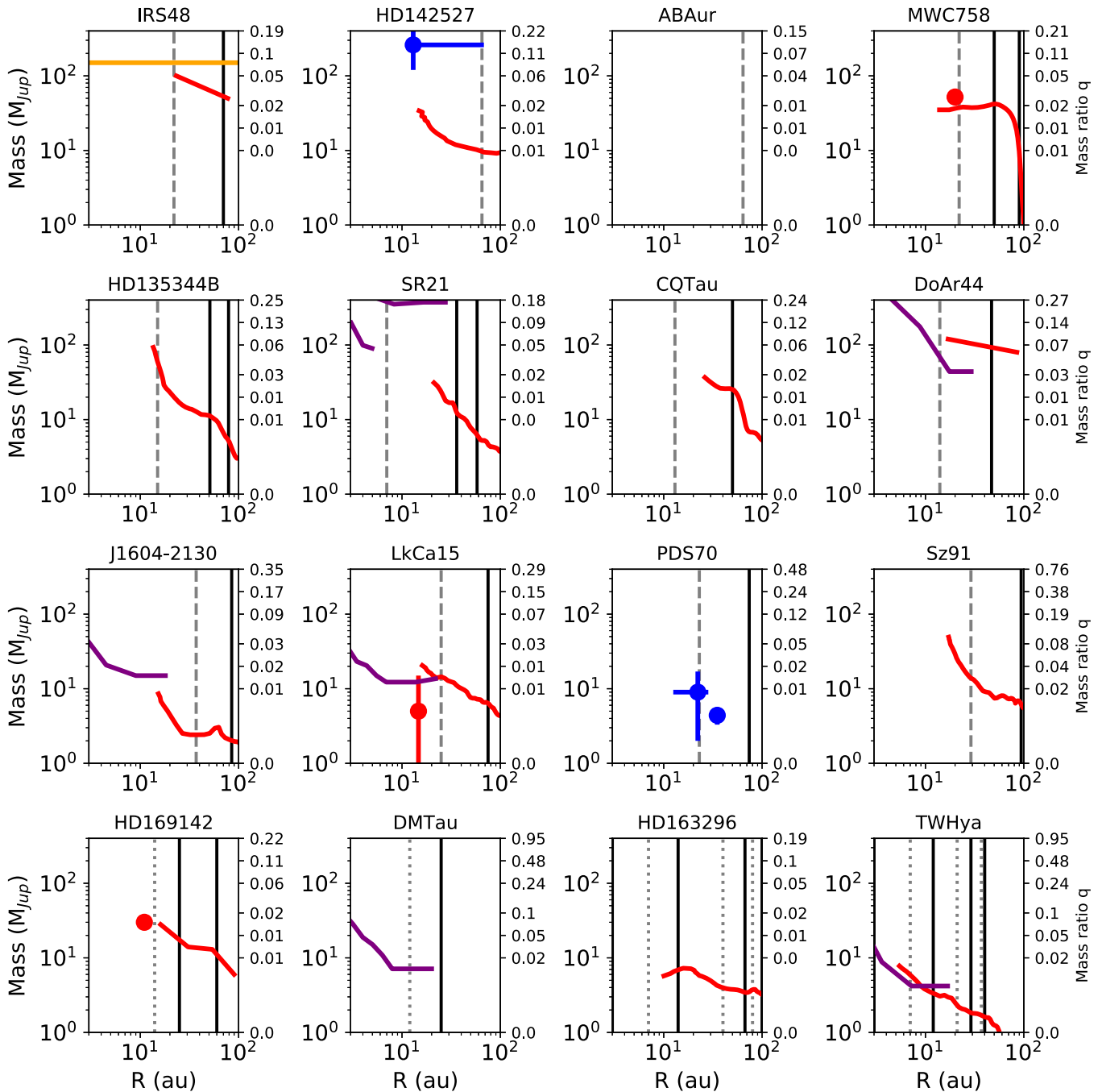
3.3. Companions

Many transition disks have been studied in direct imaging searches for embedded companions. Figure 4 presents the best known limits for companions in the disks in our sample, in comparison with the locations of the dust rings and gas gaps. The right y-axis provides the mass ratio with respect to the stellar mass in percentage. References for high-contrast direct

imaging searches are provided in Table 2, and additional data are discussed below. The mass upper-limit curves are computed in these works by comparing the brightness limit with evolutionary models such as BT-SETTL (Allard 2014) or COND (Baraffe et al. 2003), assuming the age of the system and hot-start models. When values for both models were computed, we adopted the BT-SETTL results. Companion detections are marked with red (unconfirmed) and blue (confirmed) circles. The evolutionary models for upper limits and most candidates do not include contributions from a circumplanetary disk (CPD), which could dominate the brightness and lower the mass limit estimates by a factor of 10 (Zhu 2015). Also, extinction, age estimate, and choice of evolutionary model may affect the derived mass estimates and limits.

For PDS 70 and LkCa 15, Hα and multiwavelength data (spectral energy distribution, SED) provide constraints on the CPD, which means that their estimated companion mass is much lower than the typical contrasts in other disks. Although the SED of HD 142527B might be explained with a planetary companion with a CPD as well (Brittain et al. 2020), the companion mass is very likely substellar based on a proper-motion study of the primary star (Claudi et al. 2019) and previous fits of the SED and SINFONI H + K spectrum to BT-SETTL models (Lacour et al. 2016; Christiaens et al. 2018).

For IRS 48, upper limits on companion brightness were measured by Ratzka et al. (2005) with speckle imaging at 0″15 and 0″5 (20 and 67 au), converted to mass limits of 100 and 50 M_{Jup} by Wright et al. (2015), which are interpolated in our contrast curve. In addition, Simon et al. (1995) measured a K-band contrast in the regime 0″02–1″ (~3–135 au) using the

Figure 4. Companion candidates and limits for each target (see Table 2 for references). Red lines show the results from coronagraph studies, purple lines show the results from sparse aperture masking studies, and the orange line is for lunar occultation (see text). Blue symbols show confirmed companions, whereas red symbols are unconfirmed candidates. The black solid lines indicate the locations of the dust rings, whereas the gray dashed lines indicate the gas gap locations as derived from the ^{13}CO in Section 3.2. Gray dotted lines indicate estimates of the gas gaps in between the dust rings.

lunar occultation method, which was converted to a mass limit of 150 M_{Jup} (Wright et al. 2015). The latter is marked with an orange line in Figure 4. Also, for DoAr 44, we add limits from Ratzka et al. (2005) converted by Wright et al. (2015). For AB Aur, no contrast curves have been derived to our knowledge. For SR 21, Sallum et al. (2019) performed a detailed analysis using sparse aperture masking detecting features around 7 au, but modeling showed that these were more consistent with an inner dust ring rather than a companion. The features require a warped inner disk or spiral features. For LkCa 15, the companion candidates c and d

identified by Sallum et al. (2015) have been suggested to originate from scattered light by inner disk material in follow-up studies (Thalmann et al. 2016; Currie et al. 2019), but we include LkCa 15b as a companion candidate due to its detection at Hα and the lack of polarized emission at its location.

In additions to the limits presented in Figure 4, we show additional constraints from a brown dwarf survey through sparse aperture masking for SR 21, DoAr 44, J1604–2130, LkCa 15, DM Tau, and TW Hya (Kraus et al. 2008, 2011; Evans et al. 2012; Cheetham et al. 2015) for the inner 0″15 of

the disk and additional limits for SR 21 for the inner 5 au (S. Sallum, private communication) using the data from Sallum et al. (2019). Unlike coronagraphy, sparse aperture masking allows the detection of companions at angular separations well within the diffraction limit down to a few au at typical disk distances (e.g., Sallum & Skemer 2019). Mass limits were derived using a range of evolutionary models using the procedure described in Kraus & Hillenbrand (2007).

A handful of indirect estimates of companion candidates are known from the literature, using a range of techniques.

1. Baines et al. (2006) claimed that AB Aur has an accreting binary companion at 82–489 au separation using Hα spectro-astrometry, which could be either inside or outside the cavity and with unknown mass.
2. Boccaletti et al. (2020) deduced a planet of 4–13 $M_{\rm Jup}$ at 30 au in AB Aur based on a spiral arm twist.
3. Gratton et al. (2019) found a tentative detection of a 3 $M_{\rm Jup}$ companion at 38 au separation in HD 169142.
4. Willson et al. (2016) found a tentative detection of a companion at 6 au separation in DM Tau using sparse aperture masking without significant sky rotation.
5. Pinte et al. (2018) and Teague et al. (2018) found evidence for ~2 $M_{\rm Jup}$ planets at 83, 137, and 260 au in HD 163296 using deviations of Keplerian motion in ^{12}CO channel maps.
6. Calcino et al. (2019) and Poblete et al. (2020) claimed substellar companions with mass ratios of ~0.2 at 10 and 30 au in IRS 48 and AB Aur, respectively, to explain the kinematics in the system.

Due to their more speculative nature, these candidates are not marked in the contrast curves in Figure 4. Follow-up observations are required to confirm their existence.

4. Analysis

4.1. Gas Gaps

In Figure 5, we present the estimated gas surface density profile, described as a Gaussian centered on $R_{\rm dust}$ and an inner width consistent with the $R_{\rm gap}$ location. Here $R_{\rm dust}$ is chosen as the outer edge of the gas gap, as the pressure maximum is thought to be located there. The $R_{\rm peak}$ is inward of $R_{\rm dust}$, but this can be understood by the radial temperature dependence; whereas the gas surface density is decreasing, the ^{13}CO emission remains partially optically thick and peaks further inward. For DM Tau and SR 21, no $R_{\rm peak}$ could be measured from the CO profile, and it was estimated to be located at ~75% of the dust ring radius. The profile is scaled to the derived gas surface density profile from the literature based on combined ^{13}CO and C^{18}O data (see references in the last column of Table 3) to match the surface density at peak, gap, and outer disk locations. The gap radii in the literature profiles were rescaled to the Gaia distances. The literature surface density profile is overplotted as a blue dotted line, and Table 3 lists the gas cavity radii $R_{\rm gascav}$ from these profiles from the literature. For PDS 70 and J1604.3–2130, the CO data were fit with a gap-like profile (material inside the companion orbit). For HD 142527 and MWC 758, the gas surface density profile was described as a Gaussian in the literature analysis (Boehler et al. 2017, 2018); $R_{\rm gascav}$ is taken as the radius where the density drops below $10^{-2}\,{\rm g\,cm^{-2}}$, where ^{12}CO becomes optically thin. For AB Aur, no detailed physical–chemical

model was used, and the CO abundance was taken to be constant throughout the disk, so the derived profile remains highly uncertain. Because TW Hya and HD 163296 do not have a resolved inner gas gap, no values are provided here. Though HD 163296 does show gas gaps in the outer disk (Isella et al. 2016), the depth and width remain highly uncertain, and we refrain from including them in the plot (van der Marel et al. 2018b).

The inner part of the gas disk remains largely unconstrained by our analysis of the CO images due to spatial resolution. We indicate the unconstrained regime with a gray area between zero and the beam radius in Figure 5. This representation reveals that, except for PDS 70, the distinction between a gas gap and gas cavity cannot be made for any of the disks. However, inner dust disks have been detected in about half of the sample (Francis & van der Marel 2020), and all disks show signs of significant gas accretion onto the star, which makes it most likely that gas is still present in the inner disk as well and the gas "cavities" are in fact gas gaps, consistent with clearing by a companion. The derived inner disk dust profiles from Francis & van der Marel (2020) and the expected gas surface density based on the accretion are included in the plot to reflect this. The expected gas surface density close to the star can be estimated indirectly assuming a viscous disk model from the stellar accretion rate by Manara et al. (2014),

$$\Sigma_g(r) = \frac{\dot{M} 2 m_p}{3\pi\alpha k_B T(r)} \sqrt{\frac{GM_*}{r^3}}, \qquad (2)$$

with $\Sigma_g(r)$ the gas surface density, $\dot{M}$ the accretion rate, m_p the proton mass, α the viscosity, k_B the Boltzmann constant, G the gravitational constant, M_* the stellar mass, and $T(r)$ the temperature profile, for which we use (Dullemond et al. 2001)

$$T(r) = \left(\frac{\phi L_*}{8\pi\sigma_B r^2}\right)^{1/4} = \sqrt[4]{\frac{\phi L_*}{8\pi\sigma_B}}\frac{1}{\sqrt{r}}, \qquad (3)$$

with L_* the stellar luminosity, ϕ the flaring angle (taken as 0.02), and σ_B the Stefan–Boltzmann constant. The stellar properties are taken from Francis & van der Marel (2020). We compute the expected local gas surface density $\Sigma_{\rm acc}$ at 1 au derived from the accretion rate assuming $\alpha = 10^{-3}$ (see Table 3) and overplot this value on the derived profiles (Figure 5).

In order to estimate the companion mass assuming a single planet, the millimeter-dust radius $R_{\rm dust}$ is compared with the derived gas gap radius $R_{\rm gap}$. Figure 6 presents this relation. Best-fit relations between the ratio and the planet mass were derived by Facchini et al. (2018b) for planet masses between 1 and 15 $M_{\rm Jup}$ for an average between $\alpha = 10^{-3}$ and 10^{-4}, but as no models were run for higher-mass companions, this relation cannot be used to estimate accurate masses for these ratios. Also, Facchini et al. did not consider eccentric orbits, which significantly increase the separation between the dust ring and the gas gap (Muley et al. 2019). The majority of our disks lie in the regime >15 $M_{\rm Jup}$, suggesting that they contain planets above this threshold, in the brown dwarf regime. The ratio between $R_{\rm dust} - R_{\rm gap}$ and $R_{\rm gap}$ for our sources is typically between 1.3 and 2.5. Outliers are CQ Tau and SR 21 with even higher ratios (3–4), suggesting very massive companions, potentially (sub)stellar.

A similar comparison was made between $R_{\rm dust}$ and the inner edge of the scattered-light gap for a sample of transition disks
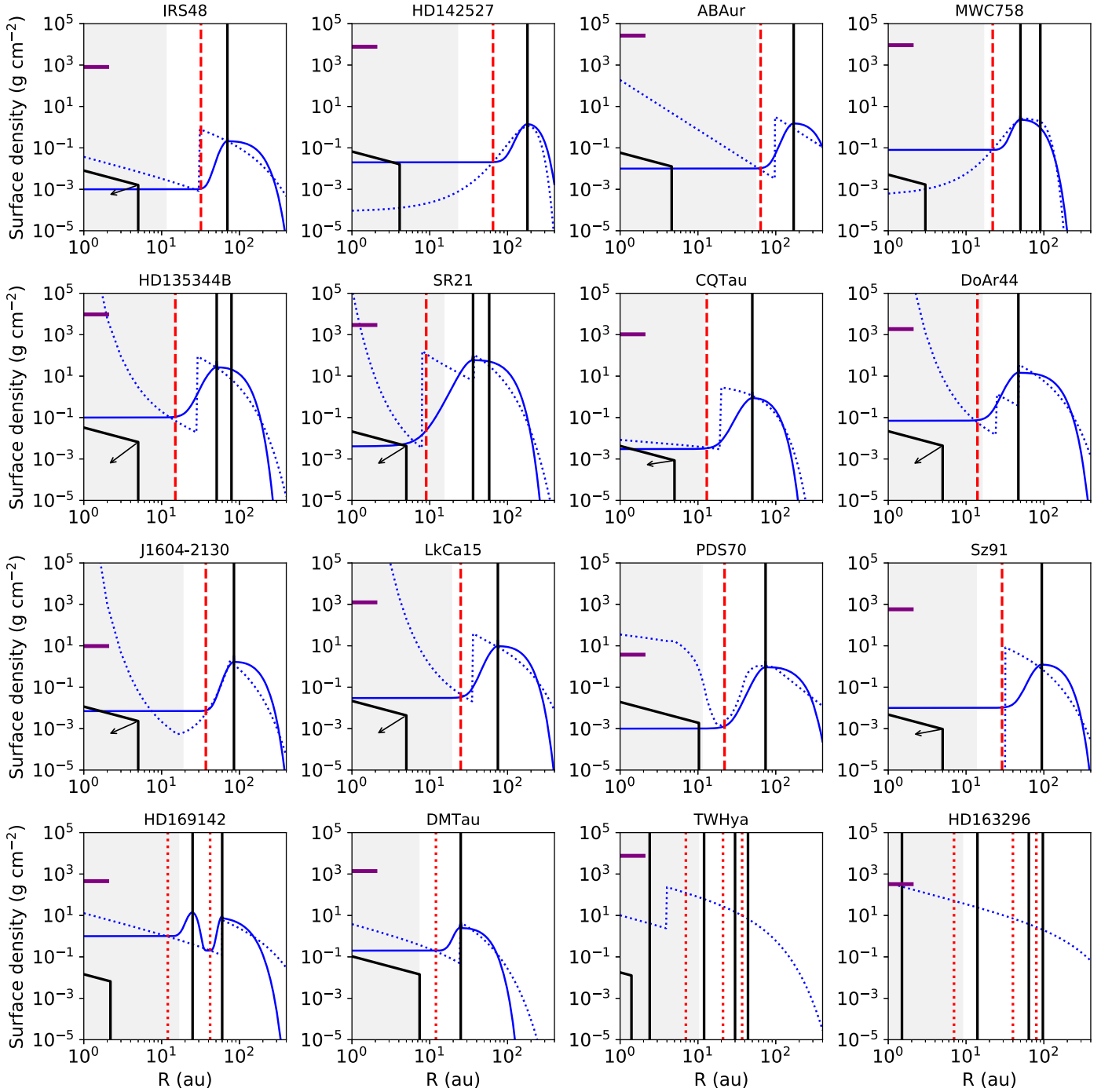
Figure 5. Estimated gas surface density profiles from our ^{13}CO analysis (blue solid lines). The blue dotted lines show the best-fit surface density profiles from the literature from a full analysis of the CO isotopologues (references in Table 3). The black solid lines indicate the dust ring locations and the inner disk dust profiles derived by Francis & van der Marel (2020). The red dashed lines indicate the location of the derived gap. The red dotted lines indicate estimates of the gas gap radii in between the dust rings. A purple marker is set at the expected gas surface density at 1 au considering the mass accretion rate of the star (see text). The gray area indicates the regime where the ALMA CO data remain unresolved (beam radius), and the gas surface density profile thus remains highly uncertain.

(Villenave et al. 2019) using the planet mass relations derived by de Juan Ovelar et al. (2013) for $\alpha = 10^{-3}$. For the overlapping targets, their estimates of companion mass are consistent with ours, with several substellar mass companions. Exceptions are IRS 48 and Sz 91, for which they used nonscattered-light observations for which the planet relation does not hold, and LkCa 15, for which the inner edge is more challenging to determine in scattered light due to its high inclination. Also, several other disks in their sample (not in our

work) that are claimed to be in the planetary regime might suffer from high inclination.

4.2. Stokes Numbers

With the azimuthal profiles fit in Appendix A and the gas surface density profiles described in Section 4.1, we construct a plot of the azimuthal FWHM as a function of the Stokes number of the traced dust grains for the radial location of the
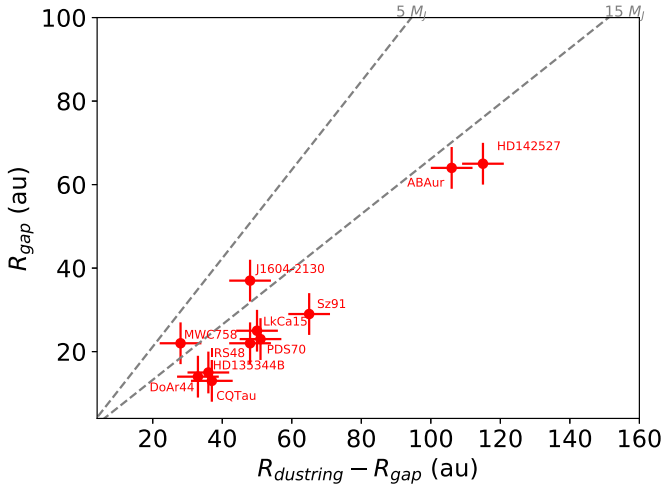
Figure 6. Gas gap vs. dust ring radius for each target, based on analysis of CO observations (see Table 2 for references). The gray dashed lines indicate the regime where the gas gap is expected to be caused by a companion of 5 and 15 M_{Jup} on a circular orbit, following the relations derived by Facchini et al. (2018b). Most disks fall below the 15 M_{Jup} line in this case and would thus have companions above that threshold, in the (sub)stellar regime.

dust. The Stokes number St as defined in Equation (1) cannot be used directly, as dust continuum emission is originating from a large range of grain sizes (and Stokes numbers). Therefore, we use a simplification with the assumption that particles with size $a_{grain} = \lambda_{obs}/2\pi$ (Draine 2006) are the primary contributors at observing wavelength λ_{obs} and introduce the observational Stokes number,

$$St_{obs} = \frac{\lambda_{obs} \rho_s}{4\Sigma_{gas}(R_{dust})}, \quad (4)$$

with the gas surface density Σ_{gas} at the location of the dust ring R_{dust}. The result is shown in Figure 7. For the uncertainties, we assume an uncertainty of a factor of 3 on $\Sigma_{gas}(r)$, based on the typical uncertainty on the gas surface density based on CO isotopologue data as derived by Woitke et al. (2019). Although other grain sizes than a_{grain} may contribute to the emission, which might add additional uncertainty, this is not considered an issue, as all Stokes numbers are computed in the same way. As it is reasonable that the grain size distributions are similar across the sample (under the assumptions that the disks have similar ages and are evolving in similar physical environments), it would thus shift all data points in the same direction, and the trend would remain the same.

Figure 7 shows that axisymmetric disks have low values of the observational Stokes number, but the asymmetric features are all located at $St_{obs} > 10^{-2}$. The derivation of gas surface density from CO isotopologue data remains uncertain, in particular due to problems with our knowledge of the carbon budget in disks (Kama et al. 2016b; Miotello et al. 2019). In addition, we show the dependence of the azimuthal contrast from the images on the observational Stokes number, which also shows a distinction between symmetric and asymmetric disks. As this trend might be affected by imaging artifacts, it is not further discussed.

To explore the physical implications of these results, we employ a model presented in Birnstiel et al. (2013) that analytically solves for the equilibrium of azimuthal drift and mixing of dust particles. The azimuthal contrast of this model

was shown to be in good agreement with the 2D calculations of Lyra & Lin (2013). Our model consists of three steps: (1) constructing a particle size distribution, (2) calculating the azimuthal equilibrium density distribution of each particle size according to Birnstiel et al. (2013), and (3) calculating the dust intensity profiles and thus the azimuthal dust intensity contrast. For the first step, the particle size distribution, we tried two different choices: first, a truncated power-law size distribution with an MRN exponent (Mathis et al. 1977) up to a maximum particle size a_{max}, and second, the steady-state distributions of Birnstiel et al. (2011). For the second step, the azimuthal density distribution, we employed Equation (8) of Birnstiel et al. (2013) and parameterized the azimuthal gas density as a constant density plus a Gaussian overdensity,

$$\Sigma_g(r, y) = \bar{\Sigma}_g(r) \frac{1 + (A - 1)e^{-\frac{y^2}{2r^2\sigma^2}}}{1 + (A - 1)\frac{\sigma}{2\sqrt{2\pi}} \text{Erf}\left(\frac{\sqrt{2}\pi}{\sigma}\right)}, \quad (5)$$

where y is the azimuthal coordinate going from zero to $2\pi r$ and σ_y is the azimuthal extent of the bump. Here $\Sigma_g(r, y)$ is normalized such that the azimuthal average gives $\Sigma_g(r)$.

The emission profile was then calculated assuming absorption opacity and a face-on, vertically isothermal disk, such that the intensity becomes $I_\nu = B_\nu(T_{dust})(1 - e^{-\tau})$, where $\tau = \sum_i \Sigma_i \kappa_{abs,i}$ is the optical depth. Here Σ_i and $\kappa_{abs,i}$ are the surface density and absorption opacity of grain size i. Optical depth is thus taken into account for the comparison with the data. The final azimuthal FWHM is computed directly for the intensity profile of the model. Although this is a rather simple approach, it is sufficient for the purpose of reproducing the trend of azimuthal extent with regard to observational Stokes number.

We explore a number of parameters, including α, gas-to-dust ratio, gas contrast, and gas azimuthal extent, and find the best fit, accompanied by two values on either side to show the dependence of the curve on the parameter (Figure 8). The threshold of the observational Stokes number where disks become asymmetric ($\sim 10^{-2}$ for most of our targets) depends on the disk properties and may vary somewhat from disk to disk. Furthermore, we explore whether the FWHM is set by fragmentation (different fragmentation velocities) or a default grain size distribution with a maximum grain size. Fragmentation velocities in lab experiments range from 1 to $10 \, \text{m s}^{-1}$ (e.g., Blum & Wurm 2008) and even higher outside the snowline (Wada et al. 2009), although the latter has been called into question by recent experiments (Steinpilz et al. 2019). The fiducial model (orange) shows a possible combination based on a manual fitting procedure: $\alpha = 10^{-3}$, gas-to-dust ratio = 10, gas contrast = 1.2, $a_{max} = 1$ mm, and azimuthal $\sigma_y = 10°$. In addition, we plot the azimuthal FWHM as a function of temperature (at the dust ring) in this figure.

4.3. Spiral Arms

A final aspect that is relevant for this discussion is the presence of spiral arms and the link with asymmetries. Table 2 indicates which disks show spiral arms in scattered light, with the references provided in the last column. About half of the sample (all asymmetric disks) shows spiral arms. For DM Tau, no scattered-light imaging data are available, and the spiral nature of HD 169142 remains uncertain, as the spiral arms are seen in total scattered light (Gratton et al. 2019) through
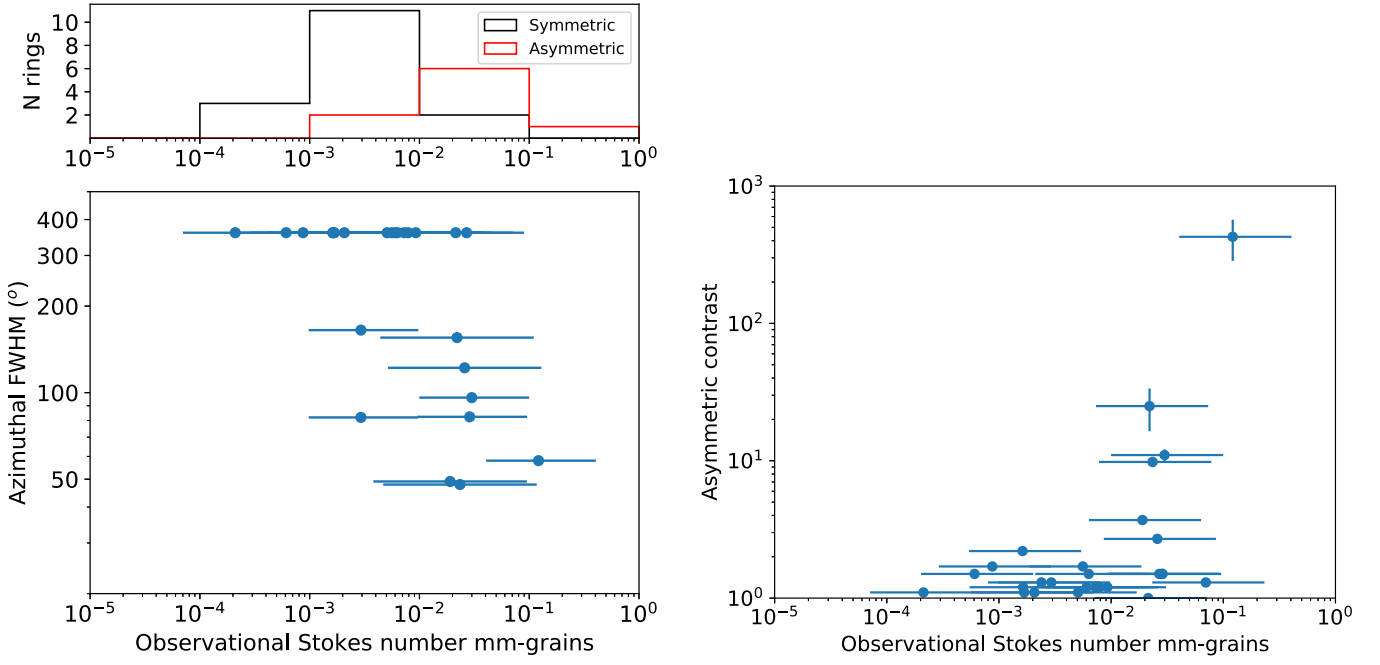
Figure 7. Left: azimuthal extent as a function of the Stokes number of millimeter grains at the location of the dust ring/asymmetry for each of our targets, computed from the visibility analysis. The Stokes number has been computed using the observing wavelength and the local gas surface density (see text for details). The top panel shows the distribution of the targets. Right: azimuthal contrast as a function of Stokes number, computed from the images.
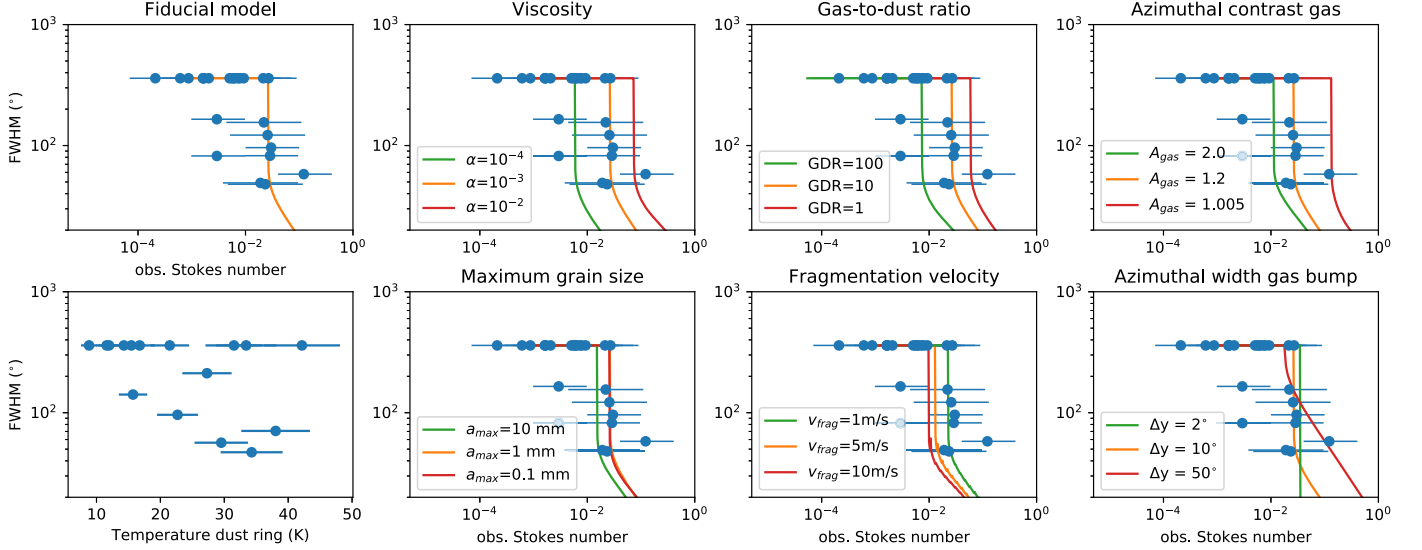
Figure 8. Azimuthal extent as a function of the observational Stokes number of millimeter grains at the location of the dust ring/asymmetry. The colored lines indicate the width expected from analytical relations of azimuthal dust trapping (Birnstiel et al. 2013) with $\alpha = 10^{-3}$ (see text). The orange line is considered to be most consistent with the data. The plot in the lower left shows the relation between the width and the temperature at the location of the dust ring.

angular differential imaging but not in polarized scattered light (Pohl et al. 2017; Bertrang et al. 2018). The former technique suffers, unlike polarized differential imaging, from possible biases deriving from the disk emission self-subtraction, in particular if the disk is seen face-on.

4.3.1. Link with Asymmetries

Garufi et al. (2018) noticed that all asymmetric disks in ALMA show spiral arms in scattered light, and the apparent origin of one of the spiral arms in HD 135344B in the dust asymmetry (van der Marel et al. 2016a) suggests that these phenomena are physically linked if a vortex triggers the spiral

arm (Lovelace & Romanova 2014). However, recent simulations show that spiral arms triggered by a vortex are unlikely to be detectable in scattered light (Huang et al. 2019), and the spirals must have a different origin, such as a companion.

Figure 9 presents a number of trend plots between the azimuthal extent and parameters that have been linked to spiral arms. The pitch angle was derived from the deprojected scattered-light images from the literature (for references, see Table 2). When no spiral arms were detected, the pitch angle is set to 1°. No difference is shown between "single" and "double" spirals, as the secondary spiral can easily be hidden in part of the disk. Ages, near-IR (NIR) excess, and stellar masses are taken from Garufi et al. (2018). For each plot, we compute
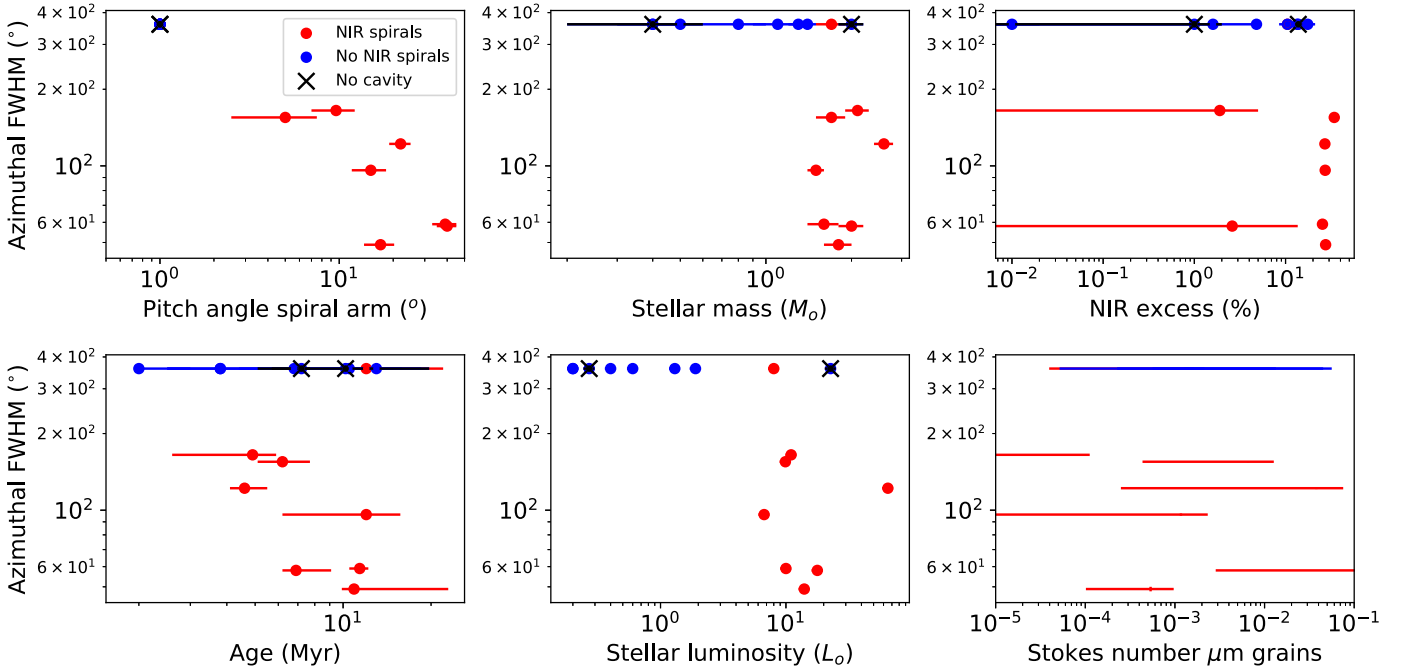
Figure 9. Relations between millimeter structure and parameters linked with spiral arms. Red data points are disks with spirals, and blue data points are disks without spirals in the NIR.

the correlation coefficient $r_{\rm corr}$ using the linear regression procedure by Kelly (2007), resulting in values of $r_{\rm corr} = 0.0 \pm 0.6$ for each plot consistent with a lack of correlation.

Although asymmetries are only seen in disks with spiral arms, as already demonstrated by Garufi et al. (2018), there is no trend between azimuthal extent and pitch angle. The pitch angle itself depends primarily on the disk temperature (hence aspect ratio) and to a lesser degree on planet mass (Fung & Dong 2015; Zhu et al. 2015). The asymmetric nature of CQ Tau is debatable, but spiral arms have been found. Asymmetries and spiral arms are only seen in stars with stellar masses $>1.5\ M_\odot$, but not exclusively; HD 163296 is an intermediate-mass star without spiral arms or azimuthal asymmetries. Disks with spirals and asymmetries exist for a range of ages within the sample, although no young disks with spiral arms or asymmetries are known. The sample is intrinsically biased, as it only contains disks with ages of $\sim$4–10 Myr, which represent a minority disk population that lives longer than the average disk lifetime of $\sim$3 Myr (Mamajek 2009). The presence of wide gaps and thus dust traps is thought to be the main reason for the longer lifetime, as radial drift is efficiently reduced (Pinilla et al. 2020). The NIR excess has been linked before to spiral arms (Garufi et al. 2018), possibly due to changes in the temperature structure in the shadows in the outer disk (Montesinos et al. 2016). Most disks with high NIR excess also show asymmetries, but not for the entire sample.

In the bottom right panel of Figure 9, we test whether the detection of spiral arms can be linked to the local gas surface density in the same way as the millimeter asymmetries through the Stokes number, following Veronesi et al. (2019). We thus aim to test whether the Stokes numbers of micron-sized dust grains are significantly different in disks with spiral arms and disks with rings in scattered light (see Table 2). In each disk, the radial range of the scattered-light features (rings and spiral arms) is estimated from the literature, and the Stokes number of

a micron-sized dust grain is computed using the gas surface density profile in that range with Equation (4). The Stokes number of the micron-sized grains is similar throughout the sample, regardless of contrast or spiral arms. An observed trend would contradict the result of Veronesi et al. (2019), who predicted that rings are only visible at (much) higher Stokes numbers at millimeter wavelengths. The presence of spiral arms might thus be unrelated to the local gas surface density.

4.3.2. Link with Gaps and Stellar Properties

We explore the link between spirals and stars further in a wider sample comparison in Figure 10, as more massive stars are generally associated with high luminosities as well. Targets are taken from the scattered-light demographics study by Garufi et al. (2018) for which high-resolution ALMA data are available in Francis & van der Marel (2020) and Andrews et al. (2018) to estimate the dust gap width. Here $R_{\rm dustgapwidth}$ is defined as $R_{\rm cav}$ for the transition disks (Francis & van der Marel 2020) and as the gap width of the inner gap in Zhang et al. (2018) for the ring disks. The assessment of the presence of spirals is primarily based on the classification by Garufi et al. (2018, Figure 1), where spirals and giants are marked as "spiral" in our sample, rings and rims as "no spiral," and faint, small, or inclined as "unconfirmed," since the detection of spirals in these disks is hindered by the observational sensitivity, angular resolution, and disk geometry, respectively. Four giants from Garufi et al. (2018) were marked by those authors as controversial due to their high inclination, which makes the detectability of spiral arms more challenging. These are marked as "unconfirmed" in our plot. All data are provided in Appendix D.

Figure 10 shows that all spiral disks lie in the upper right corner of the diagram, with high luminosity and a large gap width, in contrast to nonspirals, with either low luminosity or a narrow gap width. This difference can be understood as the detectability of spiral arms increases with pitch angle; the pitch
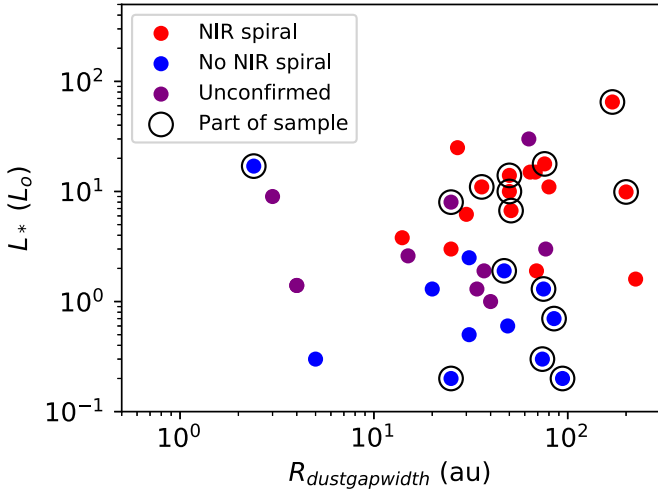
Figure 10. Comparison of luminosity, dust gap width, and the presence of spirals. The dust gap width represents the inner cavity size for transition disks or the gap width of the innermost gap in ring disks. This plot represents a larger data set including all disks imaged in scattered light from Garufi et al. (2018) for which ALMA data are available in Francis & van der Marel (2020) and Andrews et al. (2018). The full table is given in Table 7. The targets from our study are circled. This plot demonstrates that spirals are only found in disks with high luminosity and a large gap width, as expected from the relation between pitch angle, disk temperature, and companion mass.

angle is correlated with the aspect ratio (disk temperature) and, to some extent, companion mass (Dong et al. 2015; Fung & Dong 2015; Zhu et al. 2015). As the disk temperature generally scales with stellar luminosity (Dullemond et al. 2001) and the gap width roughly with companion mass (Varnière et al. 2004), the pitch angle is expected to be larger for more luminous disks with the most massive companions. This link supports a view where the scarcity of spirals around T Tauri stars is due to their low luminosity rather than their young age (Garufi et al. 2020). A larger pitch angle is more easily resolved and thus more likely to be detectable in NIR observations at low inclination. High inclination angles make the detectability of spiral arms more challenging (Dong et al. 2016), and indeed, the three purple data points in the upper right corner of Figure 10 are all disks with inclination $i \sim 40°–75°$. The two almost face-on disks with tightly wound spirals and a large empty cavity (HD 142527 and GG Tau) may remain a separate category, as these are the only confirmed binaries in this comparison. Another possible connection is that more luminous stars are generally also more massive, and higher-mass stars are more likely to have a binary companion (Raghavan et al. 2010), although binary companions have not been detected yet in the majority of these disks (see Section 3.3).

This result demonstrates that spiral arms are possibly present in all disks with gaps, assuming all gaps are opened by planets, but only detected when the planet is sufficiently massive, the star sufficiently luminous, and the inclination angle not too high. This explains why spirals are uniquely found in low-inclination disks with wide gaps and a high-luminosity star. The thresholds appears to be at $L_* \gtrsim 1.5\ L_\odot$ and $R_{\mathrm{gapwidth}} \gtrsim 15$ au, but more data are required to confirm this.

4.3.3. Link with Morphology

This connection between detectability, luminosity, and gap width thus explains the locations of the spiral disks in Figure 9 in mass and luminosity, but the link with azimuthal extent

remains unclear. Figure 11 presents an overlay of scattered-light images and ALMA data. The spiral arm(s) and dust asymmetries appear to be spatially connected, suggesting that the spiral arm and dust asymmetry may be physically related. Such a comparison has been made before for IRS 48 (Follette et al. 2015, Figure 12), MWC 758 (Dong et al. 2018b, Figure 1 (c)), HD 135344B (Cazzoletti et al. 2018, Figure 1(b)), SR 21 (Muro-Arena et al. 2020, Figure 3(d)), and CQ Tau (Uyama et al. 2020, Figure 4) for the disks in our sample, but also for, e.g., V1247 Ori (Kraus et al. 2017, Figure 1(b)) and HD 100453 (Rosotti et al. 2020, Figure 5). Proposed scenarios for these connections include, e.g., the launching of a spiral by the vortex (van der Marel et al. 2016a) and the detection of part of the spiral in millimeter emission (e.g., Rosotti et al. 2020).

No physical connection is visible in HD 142527 (Avenhaus et al. 2017), AB Aur (Tang et al. 2017), GG Tau (Keppler et al. 2020), or HD 143006 (Pérez et al. 2018), but this could be related to the limited detectability of the spiral arms in these systems around the radius of the dust asymmetry.

5. Discussion

5.1. Diversity Asymmetries

In Section 4.2, we compared the azimuthal extents of the dust asymmetries with the local gas surface density through the observational Stokes number and found a steplike trend that can be matched to a simple dust evolution model with an azimuthal pressure bump in the gas. This result suggests that the diversity of asymmetries and nonasymmetries is not linked to the disk, the companion, or a limited lifetime but rather to the local gas surface density at the location of the pressure bump. This implies that minor azimuthal pressure bumps may be very common in disks, but they are only detected as dust asymmetries when the Stokes number is sufficiently high, i.e., when the local gas surface density is sufficiently low. This also leads to the prediction that dust observations at centimeter wavelengths, such as the ngVLA, will show a much larger number of asymmetric disks, as a higher observational Stokes number is traced at these wavelengths.

This scenario also explains the existence of dust asymmetries in outer rings, such as seen in, e.g., HD 135344B (this study) but also V1247 Ori (Kraus et al. 2017) and HD 143006 (Andrews et al. 2018), which were not included in this study due to a lack of gas analysis. Furthermore, a dust feature identified in high-resolution data of TW Hya at 1.3 mm at 52 au was interpreted as either a CPD or a small azimuthal dust trap (Tsukagoshi et al. 2019). Our data have insufficient sensitivity to reveal this feature. The Stokes number (using our gas surface density profile) is ∼0.3 at the location of the feature, which follows the same trend as the other data points in Figure 7, and the feature could thus indeed be another azimuthal dust trap. As there are no clear correlations between azimuthal extent and typical spiral arm properties (Figure 9), asymmetries may be unrelated to the location or mass of the companion.

If this scenario is correct, asymmetries are not related to the lifetime of a vortex or gas horseshoe. Previous studies have suggested that vortices dissipate on relatively short timescales due to dust feedback (Fu et al. 2014; Miranda et al. 2017), although 3D simulations do not reproduce rapid vortex dissipation (Lyra et al. 2018). Hammer et al. (2017) showed that vortices induced by planets may have limited lifetimes when the planet mass growth is not sufficiently fast. Both
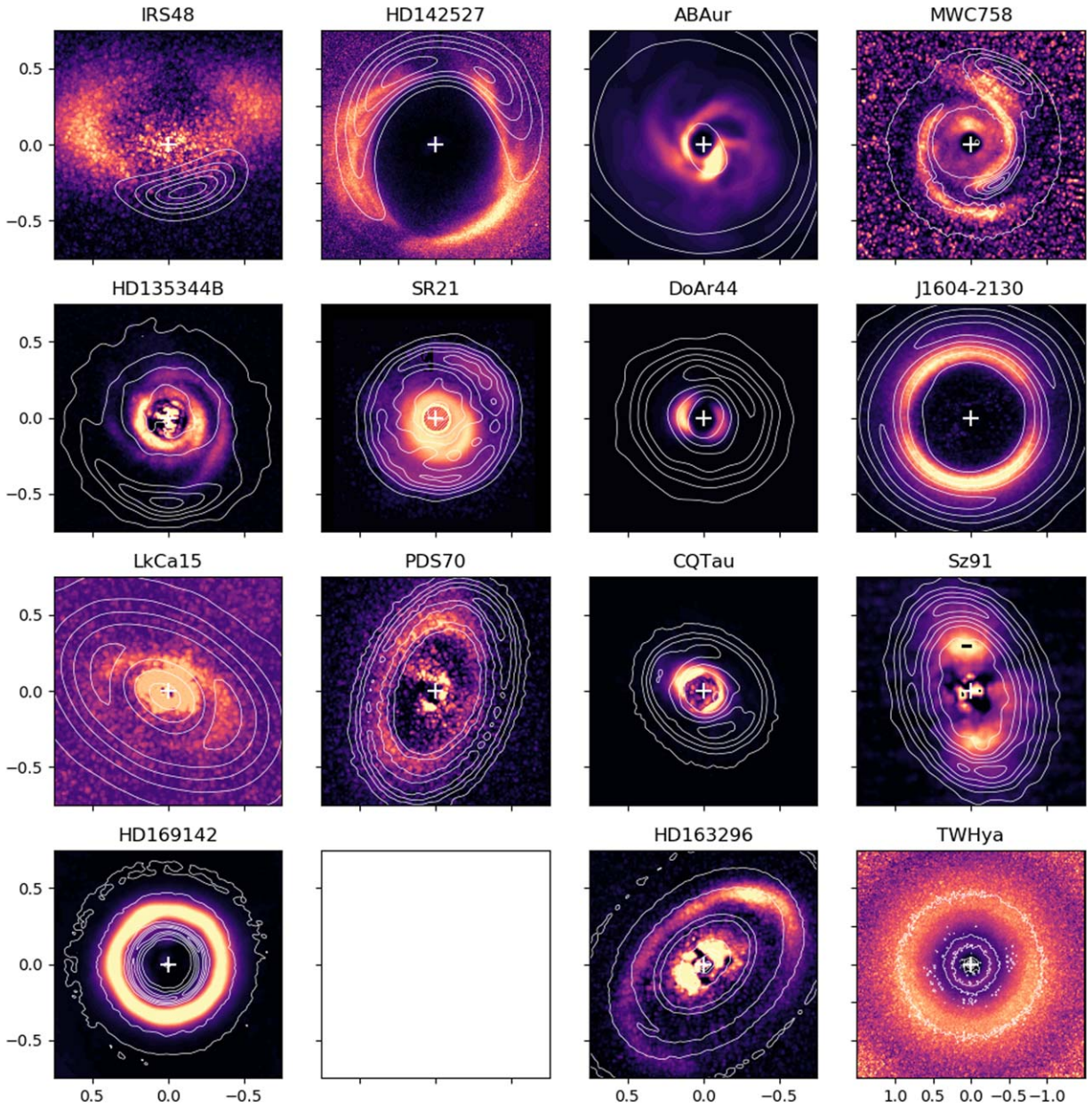
Figure 11. Overlay of ALMA millimeter continuum (white contours) onto optical/NIR scattered-light images (colors). Most images are from SPHERE/IRDIS, except IRS 48 and CQ Tau (HiCIAO), HD 142527 and HD 135344B (ZIMPOL), and Sz 91 (NaCo). No NIR image is available for DM Tau. Here HD 142527 and TW Hya are zoomed out compared to the other plots because of their angular size. The bands and references are as follows. IRS 48: H band (Follette et al. 2015); HD 142527: I band (Avenhaus et al. 2017); AB Aur: H band (Boccaletti et al. 2020); MWC 758: Y band (Benisty et al. 2015); HD 135344B: I band (Stolker et al. 2016); SR 21: H band (Muro-Arena et al. 2020); DoAr 44: H band (Avenhaus et al. 2018); J1604–2130: J band (Pinilla et al. 2018a); LkCa 15: J band (Thalmann et al. 2016); PDS 70: J band (Keppler et al. 2018); CQ Tau: H band r^2 scaled (Uyama et al. 2020); Sz 91: K band (Maucó et al. 2020); HD 169142: J band (Pohl et al. 2017); HD 163296: H band (Muro-Arena et al. 2018); TW Hya: H band (van Boekel et al. 2017).

scenarios have been used to argue that the occurrence rate of asymmetries is caused by the limited lifetime. Our work demonstrates that a timescale may be irrelevant for the occurrence rate. This implies that dissipation of vortices and/or horseshoes could happen on much longer timescales than the lifetime of the disk.

Figure 8 also shows typical values for the gas overdensity consistent with the observations. Several parameters are redundant with each other; a lower viscosity requires a lower gas overdensity and/or gas-to-dust ratio. As vortices are thought to survive only when $\alpha \lesssim 10^{-4}$ (de Val-Borro et al. 2007), this implies that for vortices, the gas-to-dust ratio is likely to be closer to unity, whereas gas horseshoes also survive

at high α and may have higher gas-to-dust ratios and/or gas overdensities. Furthermore, the extent dependence becomes shallower for a wider azimuthal width of the gas bump.

Another interesting aspect is the choice of the dust grain size distribution. Both the equilibrium model using a fragmentation velocity and a grain size distribution with a fixed maximum grain size can reproduce the curve. This means that we can neither rule out nor confirm that fragmentation of grains is the limiting effect for dust growth inside the dust trap. Future multiwavelength data might be able to probe the material properties of these dust particles. In the fragmentation limit, the maximum Stokes number should be inversely proportional to $\alpha \cdot T$ (Birnstiel et al. 2011), but the measured asymmetric

contrast does not show a clear dependence on the temperature (Figure 8); linear regression analysis results in an r_{corr} coefficient of -0.3 ± 0.4.

5.2. Horseshoe, RWI, or Spiral?

The scenario described in Section 5.1 where dust asymmetries are linked to the local gas surface densities leaves the question of the origin of the gas asymmetry open. Gas horseshoes only appear at the inner edge of a wide eccentric gap and are unable to trigger secondary asymmetries, so they can be excluded for asymmetries in disks with multiple rings with asymmetries and multiple asymmetries, such as seen in SR 21 and CQ Tau. The disks with single dust rings and asymmetric features (HD 142527, IRS 48, and AB Aur) could still be explained by either gas horseshoes or vortices as the result of RWI.

The main distinctions between the gas horseshoe and vortex scenarios are the disk viscosity and the mass of the companion; vortices require $\alpha \lesssim 10^{-4}$ to survive for a sufficient amount of time (e.g., Godon & Livio 1999; Regály et al. 2012), whereas the gas horseshoe can exist at higher α, and an RWI occurs at the edge of a planet gap as long as the planet is massive enough to carve a deep gap ($\gtrsim 1 \, M_{Jup}$), whereas the gas horseshoe requires a mass ratio $q > 0.05$, corresponding to $\gtrsim 50$–100 M_{Jup} for 1–2 $M_\odot$ stellar mass. The RWI also develops at the edge of an eccentric gap as long as $\alpha \lesssim 10^{-4}$ (Ataiee et al. 2013). The companion in the HD 142527 system has been estimated to be ~ 150–440 M_{Jup} or $q = 0.07$–0.21, consistent with the horseshoe scenario (Price et al. 2018), but in other disks, no such companion has been identified. As the viscosity remains very challenging to constrain observationally, the companion mass provides the best constraint on the origin of the single dust asymmetries. The possible companion masses are discussed in the next section.

For the disks with multiple rings and asymmetric features, a vortex remains a likely explanation under the assumption that disks have a viscosity $\alpha \lesssim 10^{-4}$. Hydrodynamic simulations show that the RWI always develops in these conditions at the edges of gaps, and vortices should be very common in disks. Our results demonstrate that the lack of detections of these vortices could simply be due to the local gas surface density.

Another possibility is that the underlying gas asymmetry is in fact part of the spiral density wave, which is supported by the physical connection between spiral arms and the millimeter-dust features discussed in Section 4.3. The reason that only a small part of the spiral arm is visible in the millimeter is that millimeter grains are only present at the edge of the planet gap, where the spiral density wave can lead to a further concentration of the dust azimuthally, but again, only when the local radial gas surface density is low enough. Small mismatches between the curve of the millimeter-dust and scattered-light features such as seen in HD 135344B (van der Marel et al. 2016a) can be understood, as the emission originates from different heights in the disk (Rosotti et al. 2020).

Spiral waves launched by a planet are rotating with respect to the background gas flow; they run over the dust particles with little time for the particles to react. Dust particles thus cannot get trapped and get carried along in spiral density waves; the timescales for dust accumulation in dust traps are at least 100 times longer than the local orbital period (Birnstiel et al. 2013). However, spiral waves still lead to changes in the pressure scale height and vertical flows, which may also lead to different spatial distributions of different particle sizes that reproduce the observed morphologies. Whether asymmetric features in the millimeter continuum really can be part of a spiral density wave remains a question.

Furthermore, it is unclear whether the disks without a clear physical connection between the spiral arm and millimeter-dust features listed above are intrinsically different (e.g., because of a substellar rather than a planetary companion) or whether these large-scale asymmetries are perhaps connected to the spiral arm after all. Spiral arms traced in high-resolution ^{12}CO observations (such as seen on larger scales in, e.g., HD 142527; Christiaens et al. 2014) might help to reveal this connection, as ^{12}CO remains visible at lower surface densities than small dust grains.

Multi-epoch observations of asymmetric millimeter-dust features in disks are required to measure their rotational speed, in order to see if they move along with the spiral (with the orbital speed of the companion) or on their own Keplerian orbit. The latter would directly rule out trapping in a spiral density wave.

5.3. Implications for Companions

Figure 4 shows the known limits for companions in each of the disks. The three confirmed companions (HD 142527B, PDS 70 b, and PDS 70 c) and three companion candidates (MWC 758 b, LkCa 15 b, and HD 169142 b) are located at or around the gas gap radii well inside the dust ring radii. The HD 142527B companion was detected at a small separation of 12 au, but orbital fitting indicates that the orbit is highly eccentric, and the companion may reach a separation of at least 57 au at apoapsis (Claudi et al. 2019), very close to the derived gas gap radius. For the 10 systems where the limits are derived through a contrast curve, the limits are known at the gas gap location for all except one system (CQ Tau), and for SR 21, the limits are very marginal at the gap location. Only AB Aur has no limits on companions. If the gap radii are overestimated and the gap radius is even closer in to the star, the contrast curves only provide limits for about half of the sample.

The contrast curves, which have been derived using hot-start models, rule out mass ratios $q > 0.05$ ($M_p > 50 \, M_{Jup}$, the minimum threshold for the formation of gas horseshoes) in the targeted regimes. Table 4 provides the limits for the possible companions and expected structure at the gap edge. However, high mass ratios are still possible in the inner parts of the disk where no contrast could be measured, which is particularly relevant for the disks where the derived gas gap radius is not covered by the contrast curve, such as CQ Tau, SR 21, AB Aur, and perhaps IRS 48. Such a high mass ratio was recently suggested for IRS 48 and AB Aur for reproducing the CO kinematics and dust contrast through a circumbinary simulation (Calcino et al. 2019; Poblete et al. 2020).

The large derived ratios between the gas gap radius and dust ring radius from Figure 6 imply minimum companion masses $>15 \, M_{Jup}$, which are in the brown dwarf and stellar regime, for the assumption that the gaps are cleared by a single companion on a circular orbit. On the other hand, the contrast curves generally rule out companion masses $>50 \, M_{Jup}$ at the gap location. This limits the companion masses (at R_{gap}) at the gap location to the brown dwarf regime. This would be consistent with the derived companion candidate masses in MWC 758 and HD 169142, although these masses remain highly

Table 4
Possible Companion Mass at Gap Radius

Target	$R_{\rm gap}$ (au) (1)	M_p ($M_{\rm Jup}$) (2)	q (3)	$R_{\rm p,c}$ (au) (4)	$M_{p,c}$ ($M_{\rm Jup}$) (5)	$q_{p,c}$ (6)	Gap Edge
IRS 48	22	$\lesssim 100$	$\lesssim 0.05$	⋯	⋯	⋯	RWI/horseshoe
HD 142527	65	$\lesssim 9.5$	$\lesssim 0.005$	18–57	270 ± 157	0.15 ± 0.08	Horseshoe
AB Aur	64	⋯	⋯	[a]	⋯	⋯	RWI/horseshoe
MWC 758	22	<38	<0.02	20	52 ± 10	0.03 ± 0.003	RWI/spiral+RWI/spiral
HD 135344B	15	<60	<0.04	⋯	⋯	⋯	Ring+RWI/spiral
SR 21	7	<352	<0.16	⋯	⋯	⋯	RWI/spiral
CQ Tau	13	⋯	⋯	⋯	⋯	⋯	Ring/RWI/spiral
DoAr 44	14	<44	<0.03	⋯	⋯	⋯	Ring
J1604–2130	37	<2.4	<0.002	⋯	⋯	⋯	Ring
LkCa 15	25	<14	<0.01	15	1–15	0.001–0.01	Ring
PDS 70	23	⋯	⋯	22, 35	5–9, 3.3–5.5	0.004–0.01	Ring
Sz 91	29	<14	<0.03	⋯	⋯	⋯	Ring
HD 169142	12	⋯	⋯	11	30 ± 2	0.017 ± 0.001	Ring
	42	<14	<0.008	38	3	0.002	Ring
DM Tau	12 < 7	<0.02	⋯	⋯	⋯	⋯	Ring
HD 163296	⋯	⋯	⋯	⋯	⋯	⋯	Ring
TW Hya	⋯	⋯	⋯	⋯	⋯	⋯	Ring

Note. Explanation of columns: (1) estimated gap radius from the ^{13}CO profile; (2) maximum companion mass at $R_{\rm gap}$ according to the contrast curve; (3) maximum mass ratio at $R_{\rm gap}$ according to the contrast curve; (4) radius of detected companion candidate(s) from direct imaging; (5) companion candidate mass estimate from direct imaging; (6) companion candidate mass ratio estimate from direct imaging.
[a] There is an estimate of 4–13 $M_{\rm Jup}$ at 30 au from the spiral twist in Boccaletti et al. (2020), but we leave this out due to its uncertain nature.

uncertain due to the lack of available data for analysis of the contributions by a CPD, if present.

On the other hand, it is very likely that simple planet–disk interaction models with a fixed orbit, such as those used by Facchini et al. (2018b), are insufficient to derive planet masses from CO-versus-dust images. A disk gap is thought to become eccentric when the mass ratio $q \gtrsim 0.003$ due to eccentric Lindblad resonances (Kley & Dirksen 2006); the back-reaction the disk exerts on the companion has been shown to grow its orbital eccentricity (e.g., Papaloizou et al. 2001; Ragusa et al. 2018), which is efficient down to super-Jovian planet masses when accretion onto the planet is included (D'Angelo et al. 2006). Muley et al. (2019) demonstrated that a proper planet–disk interaction model with a single planet, including accretion onto the planet and migration, is able to reproduce the observed gas gap and dust ring in PDS 70 with a planet with a mass of $\sim 4\ M_{\rm Jup}$ after 4 Myr, with a natural eccentricity growth up to $e \sim 0.3$. This simulation was run to explain PDS 70 with only PDS 70 b, as PDS 70 c was still unknown at the time. This scenario has recently been proposed to explain MWC 758 as well (Calcino et al. 2020).

We hypothesize that the wide transition disk cavities in our sample are also caused by eccentric, super-Jovian planets; these planets are in the 3–15 $M_{\rm Jup}$ regime, and their eccentric orbits have developed naturally, as shown in Muley et al. (2019). Due to the eccentric planet orbit, the disk may no longer appear eccentric. Eccentric disk cavities have been observed in MWC 758 (Dong et al. 2018b) and AB Aur (this work) but are generally hard to determine observationally. The main motivation for this scenario is thus the large separation between the dust cavity radius and the deduced gas gap, which is thought to be representative of the companion orbit. Also note that brown dwarfs are expected to carve eccentric gaps considering their high mass ratios. It is also possible that multiple companions (such as seen in PDS 70) are responsible

for the wide gaps. The (sub)stellar companions required for gas horseshoes are ruled out in the majority of our disks, with the exception of IRS 48, HD 142527, AB Aur, and CQ Tau.

The occurrence rate of massive companions from direct imaging surveys in older systems argues against brown dwarf companions as a common explanation for transition disks. Super-Jovians (5–13 $M_{\rm Jup}$) have an occurrence rate of 8.9% at 10–100 au for intermediate-mass (1.5–5 $M_\odot$) stars (Nielsen et al. 2019), which is the stellar mass range of the majority of our sample. Above that mass threshold, the occurrence rate of brown dwarfs (13–80 $M_{\rm Jup}$) at wide orbits is much lower ($\sim 1\%$, also known as the "brown dwarf desert"; Nielsen et al. 2019), but the occurrence of stellar companions ($>80\ M_{\rm Jup}$) or a binarity rate at 10–100 au is again increased, with a fraction of $\sim 15\%$ in the 1–2 $M_\odot$ stellar mass range (Moe & Kratter 2019). This suggests that transition disks are more likely caused by super-Jovians or stellar companions than brown dwarfs.

The narrow gaps in HD 163296 and TW Hya are consistent with lower-mass planets, $<5\ M_{\rm Jup}$, for which eccentricity is unlikely to develop. This is possibly a distinction between so-called transition disks and ring disks (van der Marel et al. 2019); wide gaps only develop when the planet is sufficiently massive to develop an eccentricity, which requires $q > 0.003$. A ring disk may host multiple lower-mass companions.

6. Conclusions

To summarize our study, we conclude the following.

1. Asymmetries in the dust appear to be linked to a low local gas surface density through the observational Stokes number.
2. Current dust and gas observations cannot distinguish between vortices (caused by planetary companions) and

gas horseshoes (caused by (sub)stellar companions with a mass ratio $q > 0.05$) in single-ring systems.

3. The link between the presence of asymmetries and local gas surface density can explain why asymmetric features in multiring systems are always seen in the outer ring.

4. The underlying gas asymmetries in multiring systems could be linked to either vortices (if $\alpha \lesssim 10^{-4}$ in disks) or spiral arms. The latter could explain the observed correlation between the presence of spiral arms and asymmetries in disks (Garufi et al. 2018).

5. The diversity in asymmetries does not require dissipation of vortices or gas horseshoes, and their lifetimes may be much longer than previously thought.

6. Current direct imaging results are consistent with super-Jovian and substellar companions at orbits well inside the dust rings as the cause of large gaps in transition disks.

7. The ratios between the dust ring radii and gas gap radii suggest that either super-Jovian (3–15 $M_{\rm Jup}$) companions on naturally occurring eccentric orbits or (sub)stellar (>15 $M_{\rm Jup}$) companions on circular orbits would be responsible for the wide gaps. (Sub)stellar companions ($q > 0.05$ or $>50 \, M_{\rm Jup}$) are ruled out by contrast curves for the majority of the sample at the gap location but remain possible for some disks at even smaller radii.

8. The detection of spiral arms in scattered-light images is linked to high-luminosity stars with wide gaps; these can be understood in terms of the pitch angle, which depends on disk temperature and companion mass. This can also explain the scarcity of detected spiral arms around T Tauri stars.

Our results predict that dust observations at centimeter wavelengths, such as the ngVLA, will show a much larger number of asymmetric features. Further studies of asymmetric and spiral features due to companions for a large grid of models to obtain predictions and observables are required to fully disentangle the origin and diversity of these features in observational data.

Appendix A
Visibility Analysis

In this appendix, we present the visibility analysis of the asymmetric disks in order to compute the FWHM of each asymmetric feature. The asymmetric disks are fit to a 2D profile $I(r, \phi)$, describing the radial and azimuthal features as Gaussians. The fitting is performed in the visibility plane comparing both the real and imaginary components using the `galario` tool set to Fourier transform and sample the model (Tazzari et al. 2018).

The disks can be described by a combination of one or two rings and asymmetries. Here HD 142527 and AB Aur are best fit with a combination of a ring and an asymmetry. This model is parameterized as follows:

$$I(r, \phi) = I_1 e^{\left(\frac{-(r-r_{c1})^2}{2r_{w1}^2}\right)} e^{\left(\frac{-(\phi-\phi_{c1})^2}{2\phi_{w1}^2}\right)} + I_2 e^{\left(\frac{-(r-r_{c2})^2}{2r_{w2}^2}\right)}$$
$$\times \, e^{\left(\frac{-(\phi-\phi_c)^2}{2\phi_w^2}\right)} + I_3 e^{\left(\frac{-(r-r_{c3})^2}{2r_{w3}^2}\right)} + I_4 e^{\left(\frac{-(r-r_{c4})^2}{2r_{w4}^2}\right)}. \quad (A1)$$

Here IRS 48 can be described by a single 2D Gaussian, where the radial profile is found to be best fit with a fourth power rather than a second power:

$$I(r, \phi) = I_1 e^{\left(\frac{-(r-r_c)^4}{2r_w^4}\right)} e^{\left(\frac{-(\phi-\phi_c)^2}{2\phi_w^2}\right)}. \quad (A2)$$

The best-fit parameters are found by careful exploration of the parameter values for initial estimates, followed by a fit to the visibilities with the Markov Chain Monte Carlo (MCMC) code `emcee` (Foreman-Mackey et al. 2013) for constraining each asymmetry. In the MCMC, 70 walkers were used in combination with 2000 steps. The position angle and inclination are fixed, taken from Table 2. The phase center is fit as well and listed in the table. The MCMC runs converge to Gaussian distributions with small statistical errors (see example in Figure 12). In particular, the statistical errors on ϕ_w (the parameter of interest) are less than 1°. The offsets at long baselines in the imaginary curve of SR 21 have low weights and do not contribute much to the fit. For HD 142527, it was not possible to find convergence, likely due to the complexity of the shadow around the peak due to the misaligned inner disk (Casassus et al. 2018). The best-fit parameters are thus not as well constrained as the other disks but sufficient for our purposes.

The best-fit models are shown in the visibility curves in Figure 13. The best-fit models are mapped onto the observed visibilities, imaged, and subtracted to image the residuals. This
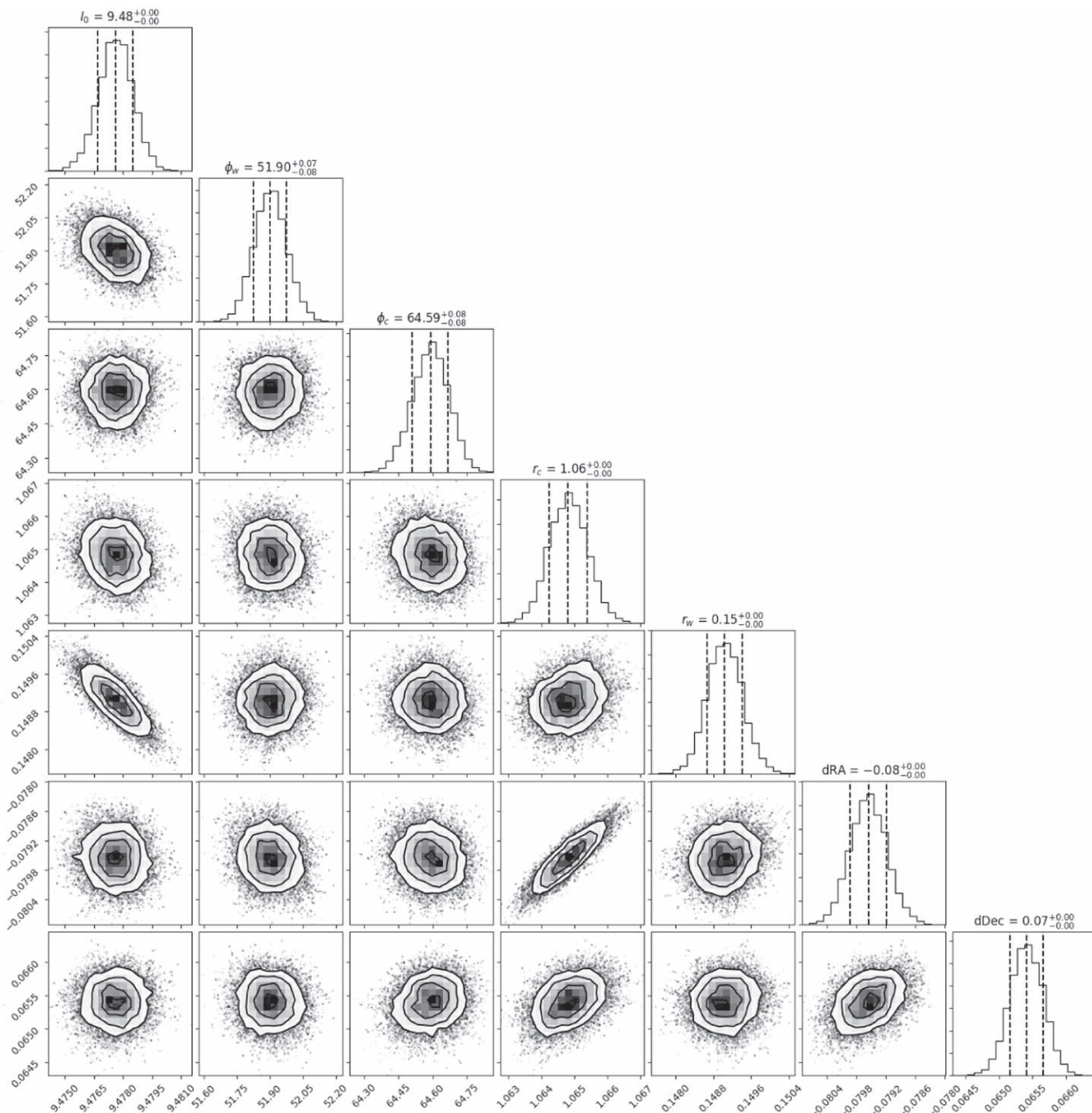
Figure 12. Example of the MCMC results for the asymmetry in AB Aur, showing the 2D posterior distributions for the MCMC fit. The median values and 1σ standard deviation of the best-fitting parameters are indicated by dashed lines.

comparison is presented in Figure 14. The residuals typically contain 12%–22% of the peak image, similar to the best fits of Cazzoletti et al. (2018) for HD 135344B. These residuals are due to the structures that cannot be well represented by a simple double Gaussian, as used to model the asymmetry. The best-fit parameter values are listed in Table 5.

The ϕ_w value provides the estimate for the FWHM of each asymmetry by multiplication with 2.36.
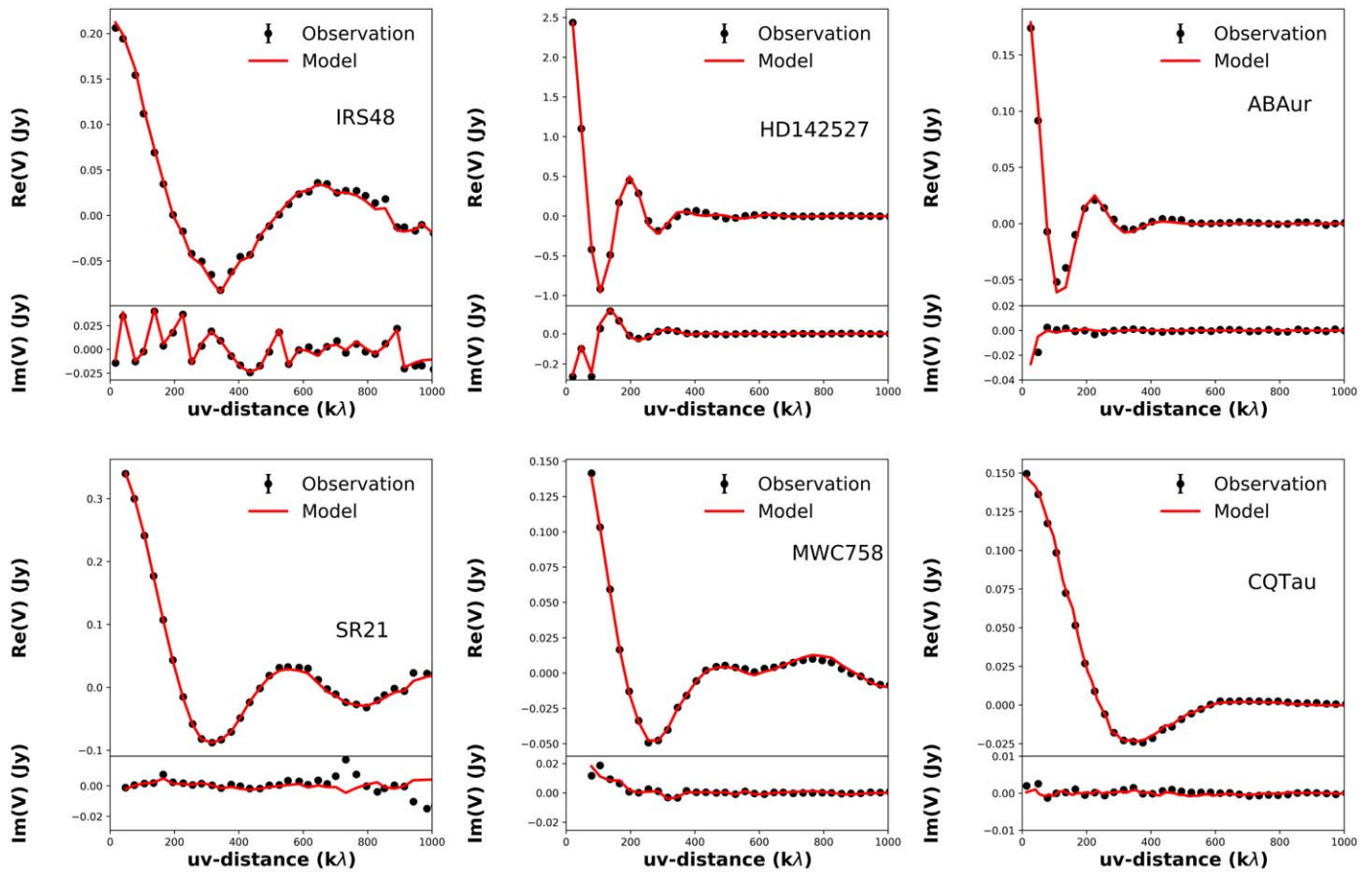
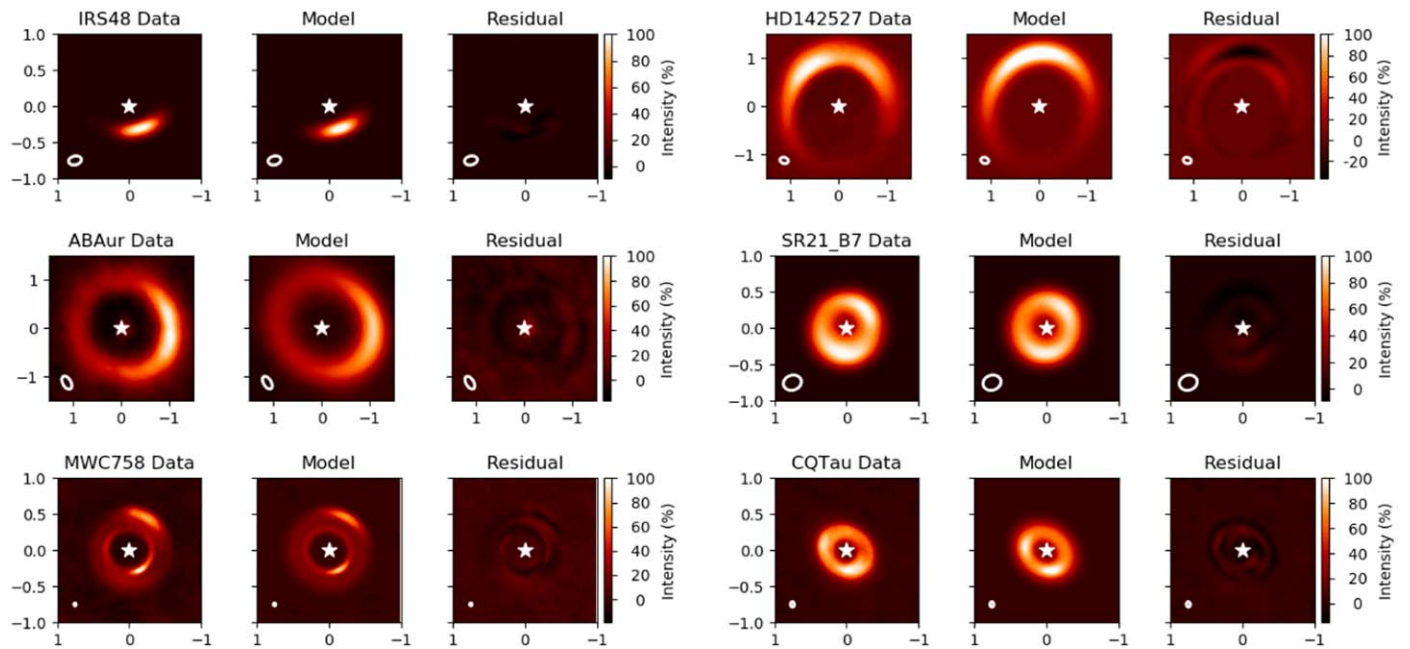**Figure 13.** Visibility curves and best-fit models (in red) of each of our asymmetric disks.

Figure 14. Best-fit models from the visibility analysis, normalized to the peak of the original image.

Table 5
Best-fit Parameters of Asymmetric Models

Parameter	IRS 48	HD 142527	AB Aur	SR 21	MWC 758	CQ Tau
$\log I_1$ (Jy sr^{-1})	11.09	10.92	9.48	10.35	10.60	9.75
r_{c1} (arcsec)	0.49	1.15	1.06	0.40	0.31	0.30
r_{w1} (arcsec)	0.10	0.22	0.25	0.06	0.02	0.05
ϕ_{c1} (deg)	165	240	65	340	123	245
ϕ_{w1} (deg)	25	66	52	35	21	24
$\log I_2$ (Jy sr^{-1})	⋯	⋯	⋯	10.35	10.55	9.90
r_{c2} (arcsec)	⋯	⋯	⋯	0.42	0.57	0.31
r_{w2} (arcsec)	⋯	⋯	⋯	0.06	0.04	0.05
ϕ_{c2} (deg)	⋯	⋯	⋯	130	360	132
ϕ_{w2} (deg)	⋯	⋯	⋯	70	20	25
$\log I_3$ (Jy sr^{-1})	⋯	⋯	9.25	10.30	10.00	10.10
r_{c3} (arcsec)	⋯	⋯	1.00	0.39	0.32	0.30
r_{w3} (arcsec)	⋯	⋯	0.25	0.06	0.03	0.12
$\log I_4$ (Jy sr^{-1})	⋯	⋯	⋯	10.45	9.85	⋯
r_{c4} (arcsec)	⋯	⋯	⋯	0.21	0.45	⋯
r_{w4} (arcsec)	⋯	⋯	⋯	0.03	0.10	⋯
R.A.	16:27:37.182	15:56:41.872	04:55:45.863	16:27:10.27	05:30:27.537	05:35:58.471
Decl.	−24:30:35.38	−42:19:23.655	+30:33:03.985	−24:19:13.068	+25:19:56.583	+24:44:53.614

Appendix B
^{13}CO Maps

In this section, we present the integrated intensity of the ^{13}CO
data of each of our targets in Figure 15.
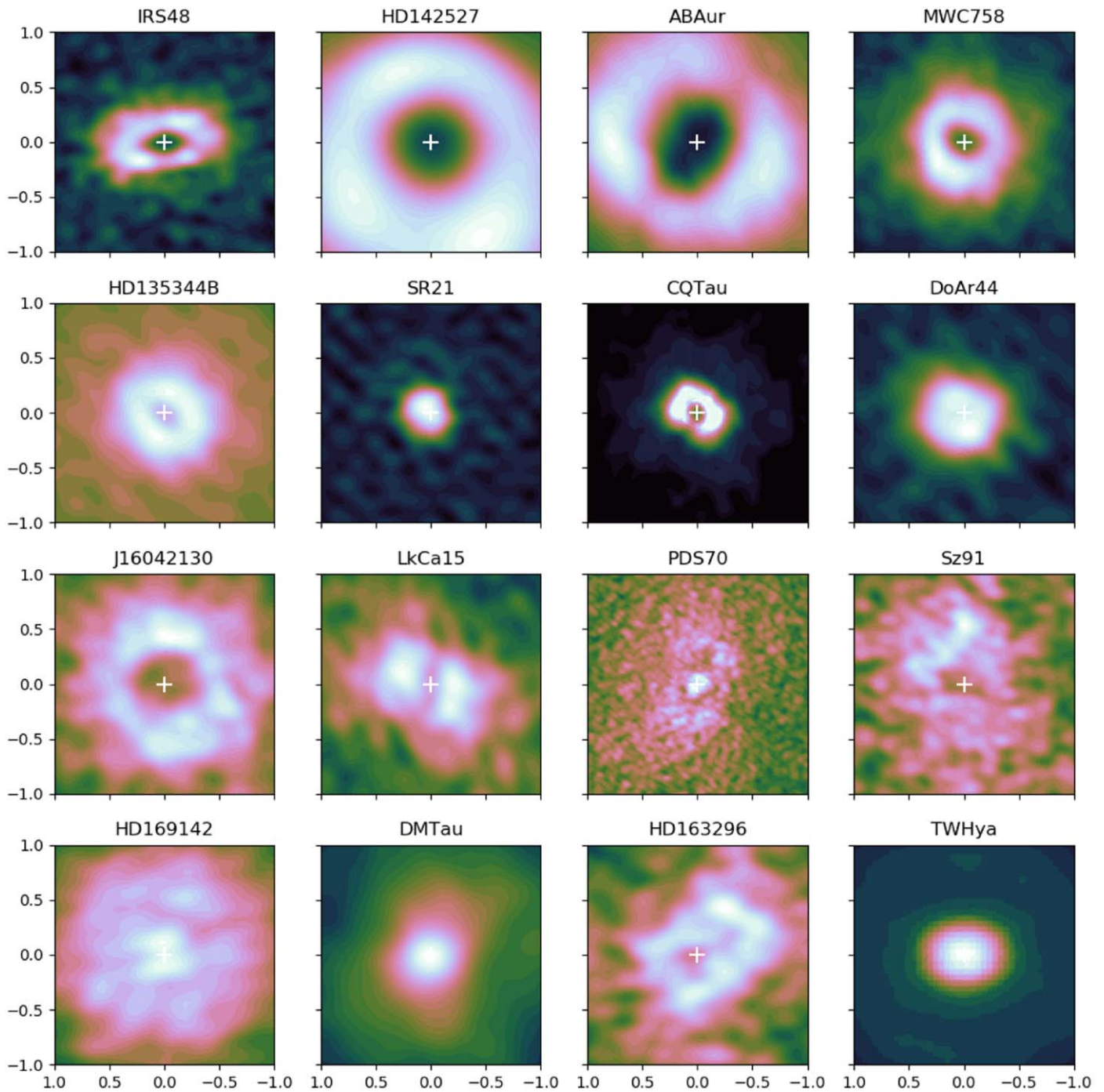
**Figure 15.** Integrated intensity maps of the ^{13}CO of each target. The title indicates which line is used.

Appendix C
Kinematics

We compare the kinematics of each disk in the first moment map of the ^{12}CO emission (Figure 16) to check for the presence of a warp, which could be an indicator of the presence of a (sub)stellar companion. We use the ^{12}CO data where available, and otherwise ^{13}CO. The properties of each moment map are summarized in Table 6.

In four disks (IRS 48, HD 142527, MWC 758, and J1604−2130), a warp is clearly detected, confirming the results from the literature (Casassus et al. 2013; Boehler et al. 2018; Mayama et al. 2018; Calcino et al. 2019). Also, AB Aur appears to show non-Keplerian motion on larger scales, but this

is most likely due to the strong contributions from the spiral arms detected in ^{12}CO (Tang et al. 2017). For Sz 91, no assessment can be made, as the ^{12}CO emission is optically thin in the inner part of the disk, and for DM Tau, the spectral resolution is very low. For the other disks, no warp is detected, but this is possibly due to the low spatial resolution compared to the location of the gap. The detectability of a warp is determined by a combination of S/N, spectral resolution, and spatial resolution compared with the companion orbit radius. Table 6 lists the relevant parameters for assessing this. We notice that the detected warps have a beam/R_{gap} value $\lesssim 1.5$ and a velocity resolution $\lesssim 0.5$ km s^{-1}, but overall, it remains challenging to determine what specifics set the detectability.
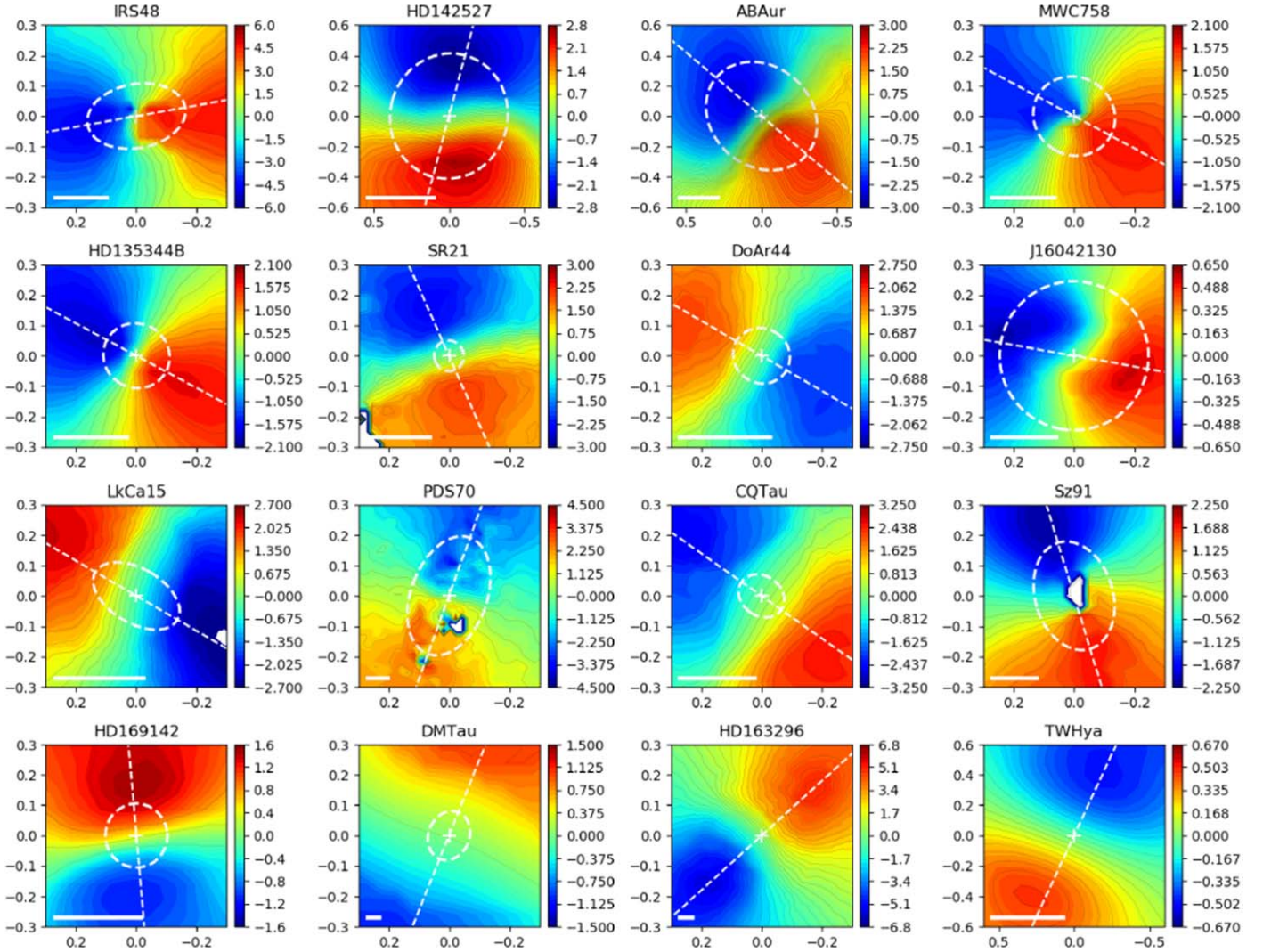
Figure 16. First moment map of each target. The colors show the gradients of the velocity, and the gray contours indicate the velocity resolution of the observations (see Table 6). The white dashed ellipses mark the gas gap radii, and the diagonal white dashed lines indicate the position angle of the outer disk to guide the eye. The images are zoomed into the central part of each disk. The horizontal bar at the bottom shows the mean diameter of the beam.

Table 6
Properties of Molecular Line Data for First Moment Maps

Target	Program	Line	Beam Size (arcsec)	Warp	Beam/R_{gap} (km s^{-1})	Δv	S/N	Other	References CO Data	References Other Signs
IRS 48	2013.1.00100.S	^{13}CO 6-5	0.19 × 0.15	Y	1.0	0.5	30	...	1	...
HD 142527	2011.0.00465.S	^{12}CO 3-2	0.55 × 0.33	Y	1.1	0.11	60	Shadows	2	3
AB Aur	2012.1.00303.S	^{12}CO 3-2	0.31 × 0.19	N?	0.6	0.2	43	Millimeter-disk	4	5
MWC 758	2012.1.00725.S	^{13}CO 3-2	0.22 × 0.19	Y	1.5	0.11	21	Millimeter-disk	6	5
HD 135344B	2012.1.00158.S	^{13}CO 3-2	0.26 × 0.21	N	2.1	0.24	23	Shadows	1	7
SR 21	2012.1.00158.S	^{13}CO 3-2	0.23 × 0.19	N	4.1	0.2	25	NIR CO	1	8
CQ Tau	2013.1.00498.S	^{12}CO 2-1	0.26 × 0.24	N	3.2	0.3	21	NIR CO	9	10
DoAr 44	2012.1.00158.S	^{13}CO 3-2	0.31 × 0.29	N	3.1	0.2	21	Shadows	1	11
J1604–2130	2015.1.00888.S	^{12}CO 3-2	0.23 × 0.19	Y	0.8	0.21	19	Variable, shadows	12	13, 14
LkCa 15	2012.1.00870.S	^{12}CO 3-2	0.36 × 0.23	N	1.9	0.21	26	Variable	15	16
PDS 70	2017.A.00006.S	^{12}CO 3-2	0.08 × 0.06	N	0.4	0.42[a]	18	Millimeter-disk	17	5
Sz 91	2012.1.00761.S	^{12}CO 3-2	0.17 × 0.13	?	0.8	0.2	27	CO?	18	19
HD 169142	2013.1.00592.S	^{12}CO 2-1	0.25 × 0.19	N	2.1	0.16	23	Millimeter-disk	20	5
DM Tau	2017.1.01460.S	^{12}CO 2-1	0.10 × 0.10	?	1.2	1.0	37	Millimeter-disk	21	5
HD 163296	2016.1.00484.L	^{12}CO 2-1	0.04 × 0.04	N	...	0.32	40	Shadows	22	23
TW Hya	2016.1.00629.S	^{12}CO 3-2	0.52 × 0.41	N	...	0.05	157	Shadows	24	25

Note. [a] Undersampled: see Keppler et al. (2019).

References. (1) van der Marel et al. (2016b), (2) Casassus et al. (2013), (3) Marino et al. (2015), (4) archival data 2012.1.00303, (5) Francis & van der Marel (2020), (6) Boehler et al. (2017), (7) Stolker et al. (2016), (8) Pontoppidan et al. (2008), (9) archival data 2013.1.00498, (10) Chapillon et al. (2008), (11) Casassus et al. (2018), (12) Mayama et al. (2018), (13) Sicilia-Aguilar et al. (2020), (14) Pinilla et al. (2018a), (15) N. van der Marel et al. (2020, in preparation), (16) Alencar et al. (2018), (17) Keppler et al. (2019), (18) van der Marel et al. (2018a), (19) Tsukagoshi et al. (2019), (20) Fedele et al. (2017), (21) Kudo et al. (2018), (22) Isella et al. (2018), (23) Muro-Arena et al. (2018), (24) Huang et al. (2018), (25) Debes et al. (2017).

Appendix D
Spiral Data

We present Table 7 that was used for creating Figure 10. Data were taken from Garufi et al. (2018), Francis & van der Marel (2020), and Zhang et al. (2018). The first 16 targets are from the sample of this study.

Table 7
Properties of Spiral and Nonspiral Disks

Target	L_* ($L_\odot$)	$R_{dustgapwidth}$ (au)	NIR Spiral?
IRS 48	17.8	76	Y
HD 142527	9.9	200	Y
AB Aur	65	170	Y
MWC 758	14	50	Y
HD 135344B	6.7	51	Y
SR 21	11	36	Y
DoAr 44	1.9	47	N
J1604–2130	0.7	85	N
LkCa 15	1.3	75	N
PDS 70	0.3	74	N
CQ Tau	10	50	Y
Sz 91	0.2	94	N
HD 169142	8	25	M
DM Tau	0.2	25	N
HD 163296	17	20	N

Table 7
(Continued)

Target	L_* ($L_\odot$)	$R_{dustgapwidth}$ (au)	NIR Spiral?
TW Hya	0.3	5	N
HD 97048	30	63	M
HD 100453	6.2	30	Y
HD 100546	25	27	Y
HD 142666	9	16	M
AK Sco	3	25	Y
GG Tau	1.6	224	Y
V4046 Sgr	0.5	31	N
LkHα 330	15	68	Y
GM Aur	1	40	M
RX J1615	1.3	20	N
V1247 Ori	15	64	Y
T Cha	1.3	34	M
AS 209	1.4	15	M
IM Lup	2.6	5	M
RU Lup	1.4	8	M
RY Lup	1.9	69	Y
CS Cha	1.9	37	M
J16083070	3	77	M
UX Tau A	2.5	31	N
J1852	0.6	49	N
HD 143006	3.8	35	Y

ORCID iDs

Nienke van der Marel ⬡ https://orcid.org/0000-0003-2458-9756
Til Birnstiel ⬡ https://orcid.org/0000-0002-1899-8783
Enrico Ragusa ⬡ https://orcid.org/0000-0001-5378-7749
Valentin Christiaens ⬡ https://orcid.org/0000-0002-0101-8814
Daniel J. Price ⬡ https://orcid.org/0000-0002-4716-4235
Steph Sallum ⬡ https://orcid.org/0000-0001-6871-6775
Logan Francis ⬡ https://orcid.org/0000-0001-8822-6327
Ruobing Dong ⬡ https://orcid.org/0000-0001-9290-7846

References

Alencar, S. H. P., Bouvier, J., Donati, J. F., et al. 2018, A&A, 620, A195
Alexander, R., Pascucci, I., Andrews, S., Armitage, P., & Cieza, L. 2014, in Protostars and Planets VI, ed. H. Beuther (Tucson, AZ: Univ Arizona Press), 475
Allard, F. 2014, in IAU Symp. 299, Exploring the Formation and Evolution of Planetary Systems, ed. M. Booth, B. C. Matthews, & J. R. Graham (Cambridge: Cambridge Univ. Press), 271
Andrews, S. M., Huang, J., Pérez, L. M., et al. 2018, ApJL, 869, L41
Andrews, S. M., Wilner, D. J., Zhu, Z., et al. 2016, ApJL, 820, L40
Ansdell, M., Gaidos, E., Williams, J. P., et al. 2016, MNRAS, 462, L101
Ataiee, S., Pinilla, P., Zsom, A., et al. 2013, A&A, 553, L3
Avenhaus, H., Quanz, S. P., Garufi, A., et al. 2018, ApJ, 863, 44
Avenhaus, H., Quanz, S. P., Schmid, H. M., et al. 2014, ApJ, 781, 87
Avenhaus, H., Quanz, S. P., Schmid, H. M., et al. 2017, AJ, 154, 33
Baines, D., Oudmaijer, R. D., Porter, J. M., & Pozzo, M. 2006, MNRAS, 367, 737
Baraffe, I., Chabrier, G., Barman, T. S., Allard, F., & Hauschildt, P. H. 2003, A&A, 402, 701
Baraffe, I., Homeier, D., Allard, F., & Chabrier, G. 2015, A&A, 577, A42
Barge, P., & Sommeria, J. 1995, A&A, 295, L1
Bate, M. R. 2018, MNRAS, 475, 5618
Benisty, M., Juhasz, A., Boccaletti, A., et al. 2015, A&A, 578, L6
Bertrang, G. H.-M., Avenhaus, H., Casassus, S., et al. 2018, MNRAS, 474, 5105
Biller, B. A., Males, J., Rodigas, T., et al. 2014, ApJL, 792, L22
Birnstiel, T., Dullemond, C. P., & Brauer, F. 2010, A&A, 513, A79
Birnstiel, T., Dullemond, C. P., & Pinilla, P. 2013, A&A, 550, L8
Birnstiel, T., Fang, M., & Johansen, A. 2016, SSRv, 205, 41
Birnstiel, T., Ormel, C. W., & Dullemond, C. P. 2011, A&A, 525, A11
Blum, J., & Wurm, G. 2008, ARA&A, 46, 21
Boccaletti, A., Di Folco, E., Pantin, E., et al. 2020, A&A, 637, L5
Boehler, Y., Ricci, L., Weaver, E., et al. 2018, ApJ, 853, 162
Boehler, Y., Weaver, E., Isella, A., et al. 2017, ApJ, 840, 60
Bosman, A. D., Banzatti, A., Bruderer, S., et al. 2019, A&A, 631, A133
Brittain, S. D., Najita, J. R., Dong, R., & Zhu, Z. 2020, ApJ, 895, 48
Bruderer, S. 2013, A&A, 559, A46
Bruderer, S., van Dishoeck, E. F., Doty, S. D., & Herczeg, G. J. 2012, A&A, 541, A91
Calcino, J., Price, D. J., Pinte, C., et al. 2019, MNRAS, 490, 2579
Calcino, J., Christiaens, V., Price, D. J., et al. 2020, MNRAS, 498, 639
Canovas, H., Hardy, A., Zurlo, A., et al. 2017, A&A, 598, A43
Casassus, S., Avenhaus, H., & Pérez, S. 2018, MNRAS, 477, 5104
Casassus, S., van der Plas, G., M, S. P., et al. 2013, Natur, 493, 191
Cazzoletti, P., van Dishoeck, E. F., Pinilla, P., et al. 2018, A&A, 619, A161
Chapillon, E., Guilloteau, S., Dutrey, A., & Piétu, V. 2008, A&A, 488, 565
Cheetham, A. C., Kraus, A. L., Ireland, M. J., et al. 2015, ApJ, 813, 83
Christiaens, V., Casassus, S., Absil, O., et al. 2018, A&A, 617, A37
Christiaens, V., Casassus, S., Perez, S., van der Plas, G., & Ménard, F. 2014, ApJL, 785, L12
Claudi, R., Maire, A. L., Mesa, D., et al. 2019, A&A, 622, A96
Currie, T., Cloutier, R., Brittain, S., et al. 2015, ApJL, 814, L27
Currie, T., Marois, C., Cieza, L., et al. 2019, ApJL, 877, L3
D'Angelo, G., Lubow, S. H., & Bate, M. R. 2006, ApJ, 652, 1698
de Juan Ovelar, M., Min, M., Dominik, C., et al. 2013, A&A, 560, A111
de Val-Borro, M., Artymowicz, P., D'Angelo, G., & Peplinski, A. 2007, A&A, 471, 1043
Debes, J. H., Poteet, C. A., Jang-Condell, H., et al. 2017, ApJ, 835, 205
Dong, R., Fung, J., & Chiang, E. 2016, ApJ, 826, 75

Dong, R., Li, S., Chiang, E., & Li, H. 2018a, ApJ, 866, 110
Dong, R., Liu, S.-y., & Fung, J. 2018b, ApJ, 860, 124
Dong, R., van der Marel, N., Hashimoto, J., et al. 2017, ApJ, 836, 201
Dong, R., Zhu, Z., Rafikov, R. R., & Stone, J. M. 2015, ApJL, 809, L5
Draine, B. T. 2006, ApJ, 636, 1114
Dullemond, C. P., Dominik, C., & Natta, A. 2001, ApJ, 560, 957
Espaillat, C., Muzerolle, J., Najita, J., et al. 2014, in Protostars and Planets VI, ed. H. Beuther et al. (Tucson, AZ: Univ. Arizona Press), 497
Evans, T. M., Ireland, M. J., Kraus, A. L., et al. 2012, ApJ, 744, 120
Facchini, S., Juhász, A., & Lodato, G. 2018a, MNRAS, 473, 4459
Facchini, S., Pinilla, P., van Dishoeck, E. F., & de Juan Ovelar, M. 2018b, A&A, 612, A104
Fedele, D., Carney, M., Hogerheijde, M. R., et al. 2017, A&A, 600, A72
Follette, K. B., Grady, C. A., Swearingen, J. R., et al. 2015, ApJ, 798, 132
Foreman-Mackey, D., Conley, A., Meierjurgen Farr, W., et al. 2013, emcee: The MCMC Hammer, Astrophysics Source Code Library, ascl:1303.002
Francis, L., & van der Marel, N. 2020, ApJ, 892, 111
Fu, W., Li, H., Lubow, S., Li, S., & Liang, E. 2014, ApJL, 795, L39
Fung, J., & Chiang, E. 2016, ApJ, 832, 105
Fung, J., & Dong, R. 2015, ApJL, 815, L21
Gaia Collaboration, Brown, A. G. A., Vallenari, A., et al. 2018, A&A, 616, A1
Garufi, A., Avenhaus, H., Pérez, S., et al. 2020, A&A, 633, A82
Garufi, A., Benisty, M., Pinilla, P., et al. 2018, A&A, 620, A94
Godon, P., & Livio, M. 1999, ApJ, 523, 350
Gratton, R., Ligi, R., Sissa, E., et al. 2019, A&A, 623, A140
Haffert, S. Y., Bohn, A. J., de Boer, J., et al. 2019, NatAs, 3, 749
Hammer, M., Kratter, K. M., & Lin, M.-K. 2017, MNRAS, 466, 3533
Huang, J., Andrews, S. M., Dullemond, C. P., et al. 2018, ApJL, 869, L42
Huang, P., Dong, R., Li, H., Li, S., & Ji, J. 2019, ApJL, 883, L39
Isella, A., Guidi, G., Testi, L., et al. 2016, PhRvL, 117, 251101
Isella, A., Huang, J., Andrews, S. M., et al. 2018, ApJL, 869, L49
Isella, A., Pérez, L. M., Carpenter, J. M., et al. 2013, ApJ, 775, 30
Kama, M., Bruderer, S., Carney, M., et al. 2016b, A&A, 588, A108
Kama, M., Bruderer, S., van Dishoeck, E. F., et al. 2016a, A&A, 592, A83
Kelly, B. C. 2007, ApJ, 665, 1489
Keppler, M., Benisty, M., Müller, A., et al. 2018, A&A, 617, A44
Keppler, M., Penzlin, A., Benisty, M., et al. 2020, A&A, 639, A62
Keppler, M., Teague, R., Bae, J., et al. 2019, A&A, 625, A118
Kley, W., & Dirksen, G. 2006, A&A, 447, 369
Kraus, A. L., & Hillenbrand, L. A. 2007, ApJ, 662, 413
Kraus, A. L., Ireland, M. J., Martinache, F., & Hillenbrand, L. A. 2011, ApJ, 731, 8
Kraus, A. L., Ireland, M. J., Martinache, F., & Lloyd, J. P. 2008, ApJ, 679, 762
Kraus, S., Kreplin, A., Fukugawa, M., et al. 2017, ApJL, 848, L11
Kudo, T., Hashimoto, J., Muto, T., et al. 2018, ApJL, 868, L5
Lacour, S., Biller, B., Cheetham, A., et al. 2016, A&A, 590, A90
Ligi, R., Vigan, A., Gratton, R., et al. 2018, MNRAS, 473, 1774
Lovelace, R. V. E., & Romanova, M. M. 2014, FlDyR, 46, 041401
Lyra, W., & Lin, M.-K. 2013, ApJ, 775, 17
Lyra, W., Raettig, N., & Klahr, H. 2018, RNAAS, 2, 195
Maire, A.-L., Stolker, T., Messina, S., et al. 2017, A&A, 601, A134
Mamajek, E. E. 2009, in AIP Conf. Ser. 1158, Exoplanets and Disks: Their Formation and Diversity, ed. T. Usuda, M. Tamura, & M. Ishii (Melville, NY: AIP), 3
Manara, C. F., Testi, L., Natta, A., et al. 2014, A&A, 568, A18
Marino, S., Perez, S., & Casassus, S. 2015, ApJL, 798, L44
Mathis, J. S., Rumpl, W., & Nordsieck, K. H. 1977, ApJ, 217, 425
Maucó, K., Olofsson, J., Canovas, H., et al. 2020, MNRAS, 492, 1531
Mayama, S., Akiyama, E., Panić, O., et al. 2018, ApJL, 868, L3
Mayama, S., Hashimoto, J., Muto, T., et al. 2012, ApJL, 760, L26
Mesa, D., Keppler, M., Cantalloube, F., et al. 2019a, A&A, 632, A25
Mesa, D., Langlois, M., Garufi, A., et al. 2019b, MNRAS, 488, 37
Miotello, A., Facchini, S., van Dishoeck, E. F., et al. 2019, A&A, 631, A69
Miranda, R., Li, H., Li, S., & Jin, S. 2017, ApJ, 835, 118
Moe, M., & Kratter, K. M. 2019, arXiv:1912.01699
Montesinos, M., Perez, S., Casassus, S., et al. 2016, ApJL, 823, L8
Muley, D., Fung, J., & van der Marel, N. 2019, ApJL, 879, L2
Müller, A., Keppler, M., Henning, T., et al. 2018, A&A, 617, L2
Muro-Arena, G. A., Dominik, C., Waters, L. B. F. M., et al. 2018, A&A, 614, A24
Muro-Arena, G. A., Ginski, C., Dominik, C., et al. 2020, A&A, 636, L4
Nielsen, E. L., De Rosa, R. J., Macintosh, B., et al. 2019, AJ, 158, 13
Owen, J. E., & Clarke, C. J. 2012, MNRAS, 426, L96
Owen, J. E., & Lai, D. 2017, MNRAS, 469, 2834
Papaloizou, J. C. B., Nelson, R. P., & Masset, F. 2001, A&A, 366, 263
Pérez, L. M., Benisty, M., Andrews, S. M., et al. 2018, ApJL, 869, L50

Pérez, S., Casassus, S., Hales, A., et al. 2020, ApJL, 889, L24
Piétu, V., Guilloteau, S., & Dutrey, A. 2005, A&A, 443, 945
Pinilla, P., Benisty, M., & Birnstiel, T. 2012, A&A, 545, A81
Pinilla, P., Benisty, M., de Boer, J., et al. 2018a, ApJ, 868, 85
Pinilla, P., Flock, M., Ovelar, M. d. J., & Birnstiel, T. 2016, A&A, 596, A81
Pinilla, P., Pascucci, I., & Marino, S. 2020, A&A, 635, A105
Pinilla, P., Tazzari, M., Pascucci, I., et al. 2018b, ApJ, 859, 32
Pinte, C., Price, D. J., Ménard, F., et al. 2018, ApJL, 860, L13
Pinte, C., van der Plas, G., Ménard, F., et al. 2019, NatAs, 3, 1109
Poblete, P. P., Calcino, J., Cuello, N., et al. 2020, MNRAS, 496, 2362
Pohl, A., Sissa, E., Langlois, M., et al. 2017, A&A, 605, A34
Pontoppidan, K. M., Blake, G. A., van Dishoeck, E. F., et al. 2008, ApJ, 684, 1323
Price, D. J., Cuello, N., Pinte, C., et al. 2018, MNRAS, 477, 1270
Qi, C., Öberg, K. I., Espaillat, C. C., et al. 2019, ApJ, 882, 160
Quanz, S. P., Amara, A., Meyer, M. R., et al. 2013, ApJL, 766, L1
Raghavan, D., McAlister, H. A., Henry, T. J., et al. 2010, ApJS, 190, 1
Ragusa, E., Alexander, R., Calcino, J., Hirsh, K., & Price, D. J. 2020, MNRAS, 499, 3362
Ragusa, E., Dipierro, G., Lodato, G., Laibe, G., & Price, D. J. 2017, MNRAS, 464, 1449
Ragusa, E., Rosotti, G., Teyssandier, J., et al. 2018, MNRAS, 474, 4460
Rameau, J., Follette, K. B., Pueyo, L., et al. 2017, AJ, 153, 244
Ratzka, T., Köhler, R., & Leinert, C. 2005, A&A, 437, 611
Regály, Z., Juhász, A., Sándor, Z., & Dullemond, C. P. 2012, MNRAS, 419, 1701
Reggiani, M., Christiaens, V., Absil, O., et al. 2018, A&A, 611, A74
Reggiani, M., Quanz, S. P., Meyer, M. R., et al. 2014, ApJL, 792, L23
Rosenfeld, K. A., Chiang, E., & Andrews, S. M. 2014, ApJ, 782, 62
Rosotti, G. P., Benisty, M., Juhász, A., et al. 2020, MNRAS, 491, 1335
Rosotti, G. P., Juhasz, A., Booth, R. A., & Clarke, C. J. 2016, MNRAS, 459, 2790
Ruane, G., Mawet, D., Kastner, J., et al. 2017, AJ, 154, 73
Sallum, S., Follette, K. B., Eisner, J. A., et al. 2015, Natur, 527, 342
Sallum, S., & Skemer, A. 2019, JATIS, 5, 018001
Sallum, S., Skemer, A. J., Eisner, J. A., et al. 2019, ApJ, 883, 100
Sicilia-Aguilar, A., Manara, C. F., de Boer, J., et al. 2020, A&A, 633, A37
Siess, L., Dufour, E., & Forestini, M. 2000, A&A, 358, 593

Simon, M., Ghez, A. M., Leinert, C., et al. 1995, ApJ, 443, 625
Steinpilz, T., Teiser, J., & Wurm, G. 2019, ApJ, 874, 60
Stolker, T., Dominik, C., Avenhaus, H., et al. 2016, A&A, 595, A113
Tang, Y.-W., Guilloteau, S., Dutrey, A., et al. 2017, ApJ, 840, 32
Tazzari, M., Beaujean, F., & Testi, L. 2018, MNRAS, 476, 4527
Teague, R., Bae, J., & Bergin, E. A. 2019, Natur, 574, 378
Teague, R., Bae, J., Bergin, E. A., Birnstiel, T., & Foreman-Mackey, D. 2018, ApJL, 860, L12
Thalmann, C., Grady, C. A., Goto, M., et al. 2010, ApJL, 718, L87
Thalmann, C., Janson, M., Garufi, A., et al. 2016, ApJL, 828, L17
Tsukagoshi, T., Muto, T., Nomura, H., et al. 2019, ApJL, 878, L8
Ubeira Gabellini, M. G., Miotello, A., Facchini, S., et al. 2019, MNRAS, 486, 4638
Uyama, T., Muto, T., Mawet, D., et al. 2020, AJ, 159, 118
van Boekel, R., Henning, T., Menu, J., et al. 2017, ApJ, 837, 132
van der Marel, N. 2017, ASSL, 445, 39
van der Marel, N., Cazzoletti, P., Pinilla, P., & Garufi, A. 2016a, ApJ, 832, 178
van der Marel, N., Dong, R., di Francesco, J., Williams, J. P., & Tobin, J. 2019, ApJ, 872, 112
van der Marel, N., van Dishoeck, E. F., Bruderer, S., et al. 2013, Sci, 340, 1199
van der Marel, N., van Dishoeck, E. F., Bruderer, S., et al. 2016b, A&A, 585, A58
van der Marel, N., Williams, J. P., Ansdell, M., et al. 2018a, ApJ, 854, 177
van der Marel, N., Williams, J. P., & Bruderer, S. 2018b, ApJL, 867, L14
Varnière, P., Quillen, A. C., & Frank, A. 2004, ApJ, 612, 1152
Veronesi, B., Lodato, G., Dipierro, G., et al. 2019, MNRAS, 489, 3758
Villenave, M., Benisty, M., Dent, W. R. F., et al. 2019, A&A, 624, A7
Wada, K., Tanaka, H., Suyama, T., Kimura, H., & Yamamoto, T. 2009, ApJ, 702, 1490
Wagner, K., Stone, J. M., Spalding, E., et al. 2019, ApJ, 882, 20
Willson, M., Kraus, S., Kluska, J., et al. 2016, A&A, 595, A9
Woitke, P., Kamp, I., Antonellini, S., et al. 2019, PASP, 131, 064301
Wright, C. M., Maddison, S. T., Wilner, D. J., et al. 2015, MNRAS, 453, 414
Zhang, S., Zhu, Z., Huang, J., et al. 2018, ApJL, 869, L47
Zhu, Z. 2015, Natur, 527, 310
Zhu, Z. 2019, MNRAS, 483, 4221
Zhu, Z., Dong, R., Stone, J. M., & Rafikov, R. R. 2015, ApJ, 813, 88
Zhu, Z., & Stone, J. M. 2014, ApJ, 795, 53